Advective gas flow in bentonite: Development and comparison of enhanced multi-phase numerical approaches

E. Tamayo-Mas [a],[*], J.F. Harrington [a], I.P. Damians [b], S. Olivella [b], E. Radeisen [c], J. Rutqvist [d], Y. Wang [e]

[a] British Geological Survey, Keyworth, Nottingham, United Kingdom
[b] Universitat Politècnica de Catalunya-BarcelonaTech and International Centre for Numerical Methods in Engineering, Barcelona, Spain
[c] Federal Institute for Geosciences and Natural Resources, Hanover, Germany
[d] Lawrence Berkeley National Laboratory, Berkeley, CA, USA
[e] Sandia National Laboratories, Albuquerque, NM, USA

ARTICLE INFO

ABSTRACT

Understanding the impact of repository gas, generated from degradation of waste and its interaction with the host rock, is essential when assessing the performance and safety function of long-term disposal systems for radioactive waste. Numerical models based on conventional multi-phase flow theory have historically been applied to predict the outcome and impact of gas flow on different repository components. However, they remain unable to describe the full complexity of the physical processes observed in water-saturated experiments (e.g., creation of dilatant pathways) and thus, the development of novel representations for their description is required when assessing fully saturated clay-based systems. This was the primary focus of Task A within the international cooperative project DECOVALEX-2019 (D-2019) and refinement of these approaches is the primary focus of this study (Task B in the current phase of DECOVALEX-2023).

This paper summarises development of enhanced numerical representations of key processes and compares the performance of each model against high-quality laboratory test data. Experimental data reveals that gas percolation in water-saturated compacted bentonite is characterised by four key features: (i) a quiescence phase, followed by (ii) the gas breakthrough, which leads to a (iii) peak value, which is then followed by (iv) a negative decay. Three models based on the multiphase flow theory have been developed. These models can provide good initial values and reasonable responses for gas breakthrough (although some of them still predict a too-smooth response). Peak gas pressure values are in general reasonably well captured, although maximum radial stress differences are observed at 48 mm from the base of the sample. Here, numerical peak values of 12.8 MPa are predicted, whereas experimental values are about 11 MPa. These models are also capable of providing a reasonable representation of the negative pressure decay following peak pressure. However, other key specific features (such as the timing of gas breakthrough) still require a better representation. The model simulations and their comparison with experimental data show that these models need to be further improved with respect to model parameter calibration, the numerical representation of spatial heterogeneities in material properties and flow localisation, and the upscaling of the related physical processes and parameters. To further understand gas flow localisation, a new conceptual model has been developed, which shows that discrete channels can possibly be induced through the instability of gas-bentonite interface during gas injection, thus providing a new perspective for modeling gas percolation in low-permeability deformable media.

1. Introduction

In all repository concepts for the geological disposal of radioactive waste, an engineered barrier system (EBS) is used to encapsulate the waste canister, or, to act as borehole or gallery seals.[1] These systems are often based on bentonite clays due to their low permeability[1–4] and high swelling capacity enabling the closure of engineering voids.[5–7] However, in all repository concepts gases will be generated through the corrosion

* Corresponding author.
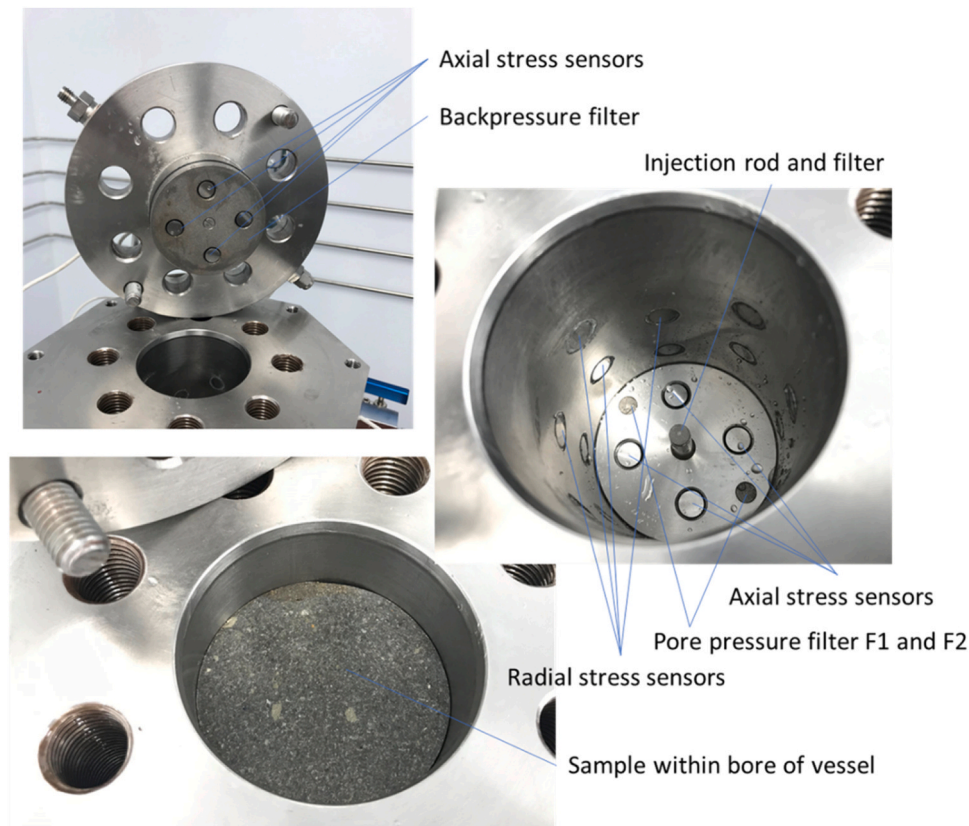*E-mail address:* elena@bgs.ac.uk (E. Tamayo-Mas).

Fig. 1. Photos of apparatus and the test sample installed within the bore of the vessel.
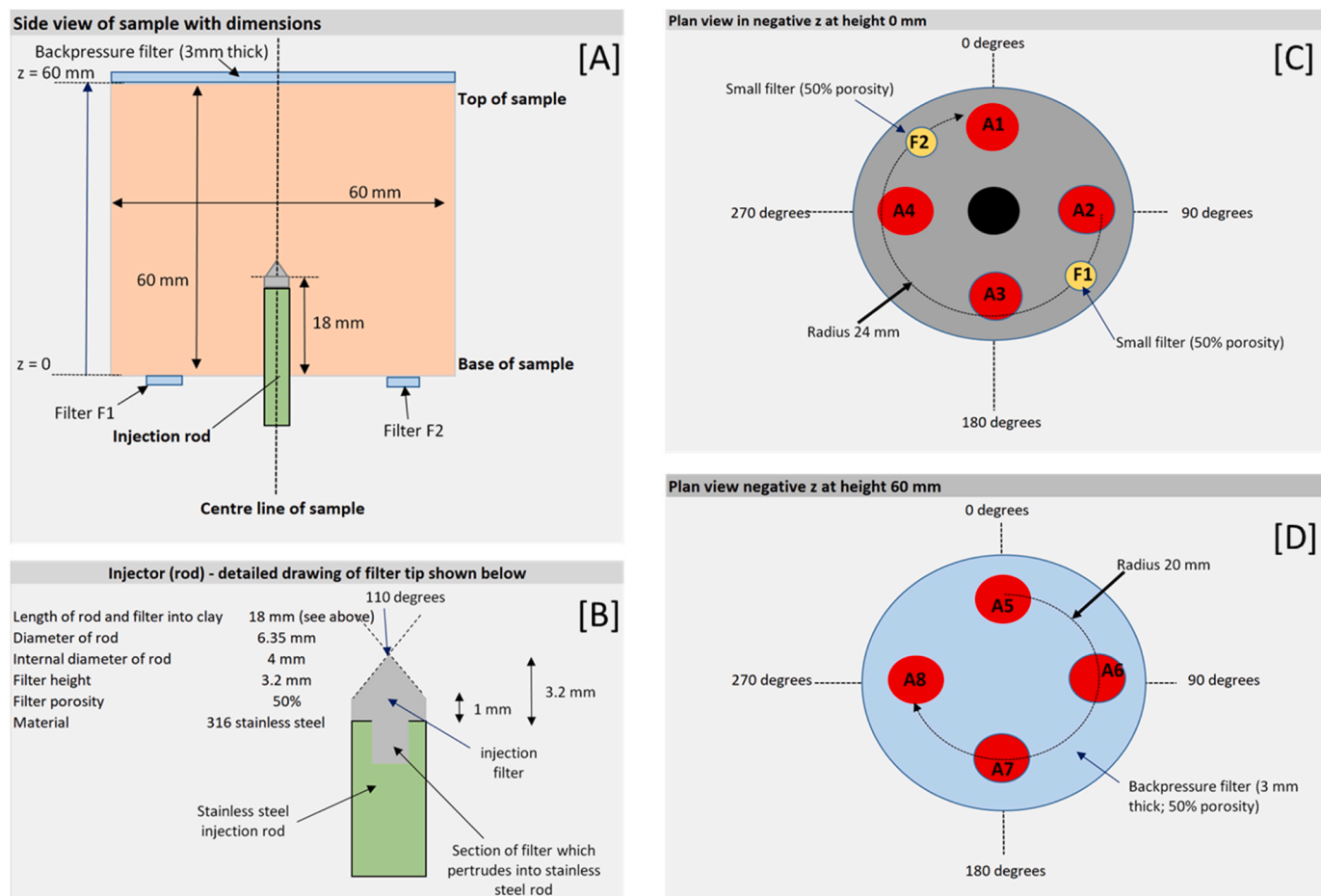
of metallic materials (under anoxic conditions), the radioactive decay of waste and the radiolysis of water.[1, 8] These gases will move by the combined processes of molecular diffusion (governed by Fick's law), solubility (governed by Henry's law) and bulk advection (described by an extended form of Darcy's law).[9] While the processes governing diffusion and solubility are well understood, the mechanisms controlling the advective movement of gas (as a discrete phase) in clay-based materials remain an active area of research. There is now a substantial body of evidence, spanning multiple decades, indicating that in these materials, gas migration occurs through the creation of dilatant pathways rather than by moving within the original porosity of the clay as conceptualised in Darcy's law.[10–19] These pathways interact with the surrounding clay mass to introduce a complex hydro-mechanical coupling.[15, 17, 20] Understanding these processes is essential to accurately modelling repository gas migration and to assess its long-term impact on the safety function of the EBS.

To this end, multiple researchers have recently developed new numerical algorithms within the framework of Biot's consolidation theory, where features such as damage, plasticity, embedded fractures, etc., have been considered to include or explicitly represent dilatant gas flow in clay-based materials.[20–26] All these models are capable of capturing some of the main response features observed in laboratory studies, but they do not appear to effectively reproduce all of the main experimental observations that characterise dilatancy-controlled flow. Indeed, although most of them can satisfactorily simulate specific experimental features such as breakthrough time, maximum pressure/stress measurements and the dilation of the sample, there remain difficulties when trying to match the whole experimental history. Features such as the evolution of stress during and after breakthrough or the temporal variations in gas outflow are not well reproduced.[21] Other features such as the improvement of parameter calibration procedures, the further development of spatially- and temporally-dependent processes and the inclusion of pathways that behave highly dynamic and unstable, still

remain uncertainties and thus, development of new and novel numerical representations for the quantitative treatment of gas in clay-based repository systems are still required. This was the primary focus of Task A in the DECOVALEX-2019 (D-2019) project,[21] in which 8 teams from around the world attempted to model advective gas flow in 1D and 3D experiments performed on compacted bentonite samples under controlled laboratory conditions.[15, 27] In Task A D-2019, four types of modelling approaches were developed: (i) two-phase flow models incorporating a range of different mechanical deformation behaviours, (ii) enhanced two-phase flow models in which fractures were embedded within a plastic material (continuous techniques) or incorporated into the model using a rigid-body-spring network (discrete approaches), (iii) a single-phase model incorporating a creep damage function in which only gas flow was considered, and (iv) a conceptual approach used to examine the chaotic nature of gas flow. In contrast to previous international gas projects such as EVEGAS[28–30] or GAMBIT,[31–33] where some model parameters were heuristically adjusted to overcome the poorly characterised couplings between the stress field and gas and water pressures, the D-2019 models featured more robust hydro-mechanical couplings based on pre-defined physical quantities. However, some of the important underlying physics (e.g., creation of dilatant pathways) associated with advective gas flow were poorly described and therefore unable to represent the full complexity of the processes in these low-permeability materials.

Several concerns were raised in Task A D-2019 as some key features in the modelling of advective gas were still unclear:

1. **Parameter calibration and model constraints**: model complexity was significantly different among the proposed strategies and some models were clearly over-parameterised. Marked differences were also found in the calibration outcomes. Indeed, both the number of the calibrated parameters and the experimental outputs used to calibrate them were significantly different between teams. While,

Fig. 2. Schematic of apparatus. [A] shows the dimensions of the sample and filters. [B] shows the dimensions of the injection filter. [C] and [D] show the location of the axial sensors in contact with the base and top of sample respectively.

some of these parameters (e.g., tensile strength, swelling pressure etc.) had a clear measurable physical meaning, others (e.g., damage smoothing coefficients, capillary spacing etc.) were numerical constructs which had an indirect physical meaning and were often unmeasurable. Hence, their definition was complex and their extrapolation to other tests was found to be difficult thus hampering the use of models as predictive tools to assess gas movement.

2. **Heterogeneity**: two models included explicit representations of material heterogeneity, but the assumed distribution functions were arbitrary. Heterogeneity might provide one possible route to represent localisation of flow in continuum models but the distribution functions could not be physically justified and thus, teams concluded that further exploration was required.

3. **Stochasticity**: the experimental data from the 1D and the 3D gas injection tests exhibited a combination of stochastic and deterministic behaviours. Gas breakthrough (identified by the discharge of gas at the backpressure filter, see Fig. 1) occurred after a period of increasing gas pressure, when bulk gas flow was observed through the development of an emergent pathway. The instability and pathway switching observed in the 3D experiment before a main flow path was established, suggested that the precise timing of the gas breakthrough and associated gas flows could be semi-stochastic in nature. It is therefore important for a deterministic analysis to understand and distinguish between the key experimental features reproducible across all experiments and those that only occur in specific experiments. Therefore, being able to analyse and model similar high-quality experimental datasets was required to help give confidence in process understanding.

4. **Upscaling**: numerically upscaling (from laboratory to field scale) poses significant challenges, which go beyond the current study. However, a future companion paper will address these issues based on an examination of a full-scale test undertaken at the Äspö Hard Rock Laboratory, Sweden.

With these concerns in mind, it was concluded that enhanced numerical representations for the quantitative treatment of gas in clay-based repository systems were required. This was the primary focus of Task B in DECOVALEX-2023 (D-2023).

This paper summarises the outcomes of stages 1 and 2 with work conducted from May 2020 to January 2022 by the four modelling teams participating in the first part of the task:

1. BGR/UFZ (Germany): Federal Institute for Geosciences and Natural Resources and the Helmholtz Centre for Environmental Research.
2. LBNL (United States of America): Lawrence Berkeley National Laboratory.
3. SNL (United States of America): Sandia National Laboratories.
4. CIMNE-UPC/Andra (Spain/France): Universitat Politècnica de Catalunya (International Centre for Numerical Methods in Engineering), funded by l'Agence nationale pour la gestion des des déchets radioactifs.

First (Section 2), a comprehensive description of the apparatus used for the test is given. Details of the test history undertaken and the new, hitherto unpublished, results can be found. Second (Section 3), team models are collated and assessed against the above-mentioned test to

Table 1

Sensor locations. Sensor prefixed with the letter A=axial and R=radial. Radius equates to the centre line of the vessel running axially along its length. Height (z) is the distance from the base of the sample. Surface area relates to the circular size of the sensor/filter, see Fig. 1.

Sensor name	Rotation (degrees)	Radius (mm)	Height, z (mm)	Surface area (mm^2)	Sensor name	Rotation (degrees)	Radius (mm)	Height, z (mm)	Surface area (mm^2)
A1	0	20	0	50.27	R10	90	30	36	50.27
A2	90	20	0	50.27	R11	180	30	36	50.27
A3	180	20	0	50.27	R12	270	30	36	50.27
A4	270	20	0	50.27	R13	45	30	48	50.27
R1	0	30	12	50.27	R14	135	30	48	50.27
R2	90	30	12	50.27	R15	225	30	48	50.27
R3	180	30	12	50.27	R16	315	30	48	50.27
R4	270	30	12	50.27	A5	0	20	60	50.27
R5	45	30	24	50.27	A6	90	20	60	50.27
R6	135	30	24	50.27	A7	180	20	60	50.27
R7	225	30	24	50.27	A8	270	20	60	50.27
R8	315	30	24	50.27	F1	135	24	0	28.27
R9	0	30	36	50.27	F2	315	24	0	28.27

Table 2

Geotechnical properties based on sample FPR-20–030.

Moisture content	Bulk density (kg/m^3)	Dry density (kg/m^3)	Void ratio	Porosity	Saturation
0.25	1989	1592	0.740	0.425	0.93

analyse their performance (Section 4). Finally, a discussion of main findings and key conclusions are provided in Sections 5 and 6 respectively. It is not the intention of this paper to provide an exhaustive description of the individual contributions from each team, but rather give a technical overview and synthesis of key conclusions and results, highlighting their main differences and similarities (see Appendix A).

2. Experimental data

As part of Task B, a new unpublished dataset was required to facilitate the comparison exercise. In previous stages of DECOVALEX-2019, teams had been given data at the outset with which to develop and calibrate their models. These experiments were based on data derived from tests performed on samples with a nominal length of 120 mm and nominal diameter of 60 mm. However, for the purposes of this numerical exercise (test FPR-21–004), the sample geometry was changed from a 2:1 ratio to a 1:1 ratio (sample of 60 mm in length and 60 mm diameter). As before, experiments were performed in a constant volume cell with material subject to rehydration first and then gas flow.

2.1. Experimental set-up

In this test geometry, the specimen is volumetrically constrained, preventing bulk dilation of the clay in any direction. This BGS custom-designed apparatus, Fig. 1, has six main components: (i) a thick-walled, dual-closure pressure vessel; (ii) an injection pressure system; (iii) a backpressure system; (iv) 24 total stress gauges to measure radial and axial total stresses; (v) two filters for monitoring porewater pressure; and (6) a data acquisition system based around a National Instruments Compact Rio set-up.

The pressure vessel comprised of a dual-closure tubular vessel manufactured from Invar (a nickel-iron alloy with a low thermal expansion coefficient, also known as Alloy 36) and was pressure-tested to 70 MPa. Each end-closure was secured by eight high tensile cap screws which could be used to apply a small pre-stress to the specimen if required. The vessel was mounted vertically with injection of gas through a rod mounted in the lower end-closure, Fig. 1, the dimensions of which are presented in Fig. 2.

The 60 mm internal bore of the pressure vessel was honed and hard-chromed to give a highly polished surface. Two pore pressure filters, labelled F1 and F2, Fig. 1, were mounted in the lower end-closure and

used to provide local measurements for pore pressure during the course of the experiment. The total stress sensors were located in a geometric pattern, Table 1, with 4 radial arrays, each comprised of four sensors, spaced evenly along the sample. Each end-closure also contained four axial total stress sensors, mounted in a square configuration, visible in Fig. 1 and Fig. 2[C] and [D].

The central or injection filter was embedded at the end of a 6.4 mm diameter stainless steel tube and was used to inject helium (see Section 2.3) during gas testing. The end of the filter was profiled to match a standard twist drill to minimize voidage around the injection tip.

Pressure and flow rate of test fluids were controlled using two ISCO-260, Series D, syringe pumps, operating from a single digital control unit. Given the potential for gas leakage past the injection pump seal, a constant flow rate was developed by displacing gas from a pre-charged cylinder by injecting water. This also helped to ensure that the helium was saturated with water vapour prior to injection, reducing the potential for desiccation. A second pre-charge vessel was placed in the backpressure circuit to collect the gas as it was discharged from the sample. Test data was over-sampled at an acquisition rate of one scan per 20 s. Thereafter, data processing was based on every 10th datapoint, unless something of note occurred within the data. All pressure transducers were calibrated to an accredited laboratory standard and linear least-squares regression fits were applied to the data to ensure its comparability.

2.2. Geotechnical properties

Geotechnical properties for the test sample FPR-21–004 were not available at the onset of the modelling exercise, as testing was still ongoing. As such, geotechnical data was provided by a second sample, FPR-20–030, manufactured in exactly the same way as that for FPR-21–004, with data presented in Table 2. Data are calculated based on a grain density of 2.77 g/cm^3.
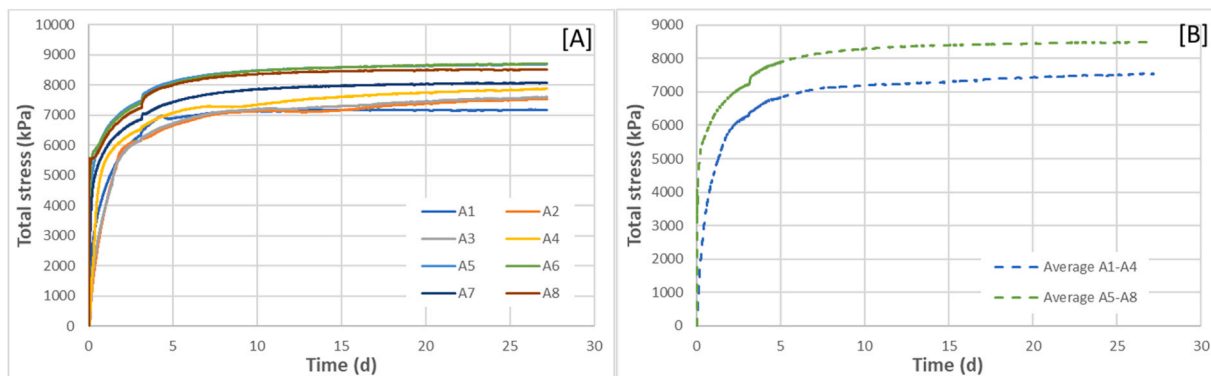
2.3. Test history

Details of each test stage are presented in Table 3. Sample FPR-21–004 was subject to a series of test stages to promote swelling and resaturation (stages 1 and 2), equilibration (stage 3) gas injection (stage 4) and self-sealing (stage 5).
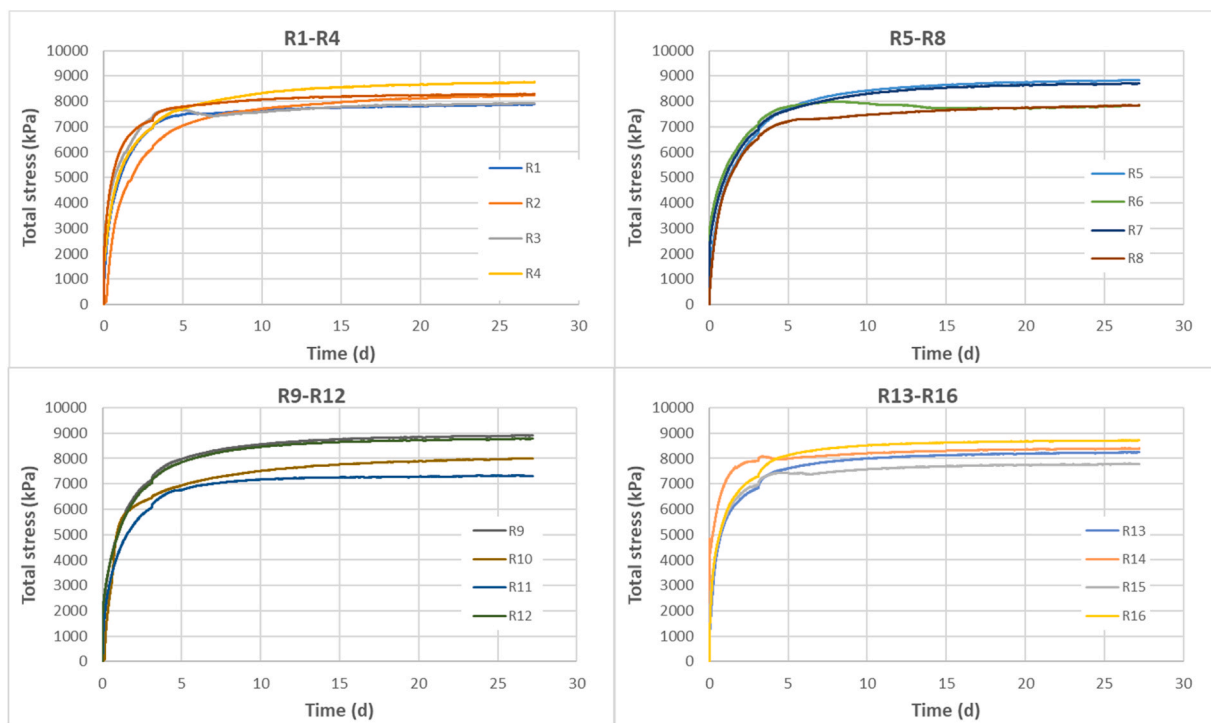
2.4. Results

Following installation of the sample, a small backpressure of 250 kPa was simultaneously applied to the backpressure filter and both F1 and F2 filters, Fig. 1. On day 3.1 (test stage 2), pressure in all three filters was increased to 1.0 MPa, and the sample allowed to hydrate. The subsequent development of axial and radial stresses is shown in Fig. 3 and

Table 3
Experimental stages and boundary conditions for test FPR-21–004.

Stage number	Stage type	Start time (d)	Injection pressure gas (kPa)	Backpressure water (kPa)	Filter F1 (kPa)	Filter F2 (kPa)	Gas displacement rate (µl/h)
1	Equilibration	0	0	250	250	250	-
2	Hydration	3.1	1000	1000	1000	1000	-
3	Equilibration	27.2	1000	1000	1000	1000	-
4	Gas ramp	28.4	2000 +	1000	-	-	180
5	Shut-in	84.9	-	1000	-	-	-

Fig. 3. Test FPR-21–004 showing the development of axial stress during test stages 1 and 2. In [A] each sensor is shown and in [B] the average stress is shown: sensors A1 to A4 (located at the base of the sample) and A5 to A8 (positioned on the top face of the sample).

Fig. 4. Test FPR-21–004 showing the development of radial stress during test stages 1 and 2. Sensors R1-R4 are closest to the base of the sample and R13-R16 are closest to the top of the sample, Table 1.
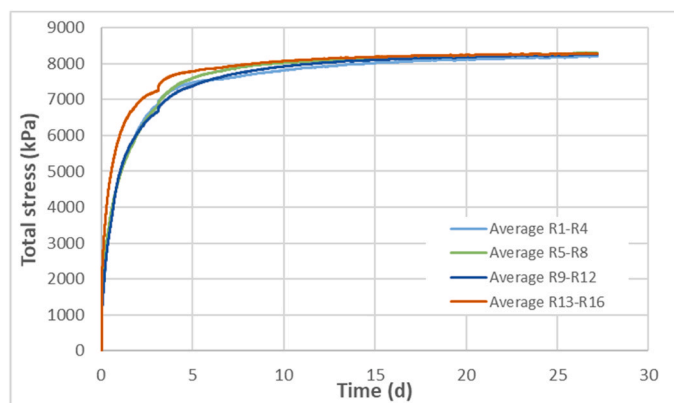
Fig. 4. At the same time, water pressure was increased and the gas (helium) pressure in the injection filter was also incremented to match the change in water pressure. This was done in order to prevent accidental water flow into the filter and thus remove the possibility of slug flow (i.e., gas displacement of water from the filter ahead of gas entry into the sample) during gas injection (stage 4).

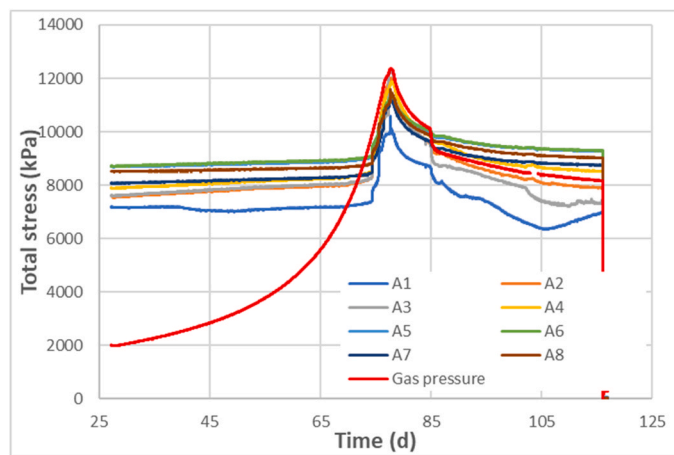Examination of the axial stress data, Fig. 3, shows a progressive increase in stress, axially throughout the sample. Unsurprisingly, stresses were systematically higher at the top of the core, adjacent to the large backpressure filter, where access to water was unlimited. At the base of the sample, access to water was limited to that available in the small filters F1 and F2, see average stresses A1-A4 in Fig. 3[B]. By the end of stage 2, this resulted in an average axial stress of 7.5 MPa, compared to 8.5 MPa at the top of the sample. Close inspection of the

Table 4
Minimum and maximum pressures at the end of stage 2 for test FPR-21–004.

Sensors	Max value at end of stage 2 (MPa)	Min. value at end of stage 2 (MPa)	Difference in pressure (MPa)
A1-A4	7.86	7.17	0.69
R16-R13	8.71	7.79	0.92
R12-R9	8.90	7.32	1.58
R8-R5	8.83	7.82	1.01
R4-R1	8.75	7.88	0.87
A5-A8	8.70	8.07	0.63

Fig. 5. Test FPR-21–004 showing the development of radial stress at each plane of measurement during test stages 1 and 2. The position of each 'array' is in Table 1.

Fig. 6. Test FPR-21–004 showing the development of gas pressure and axial stress, stage 5. The gradual increase in most sensors from day 28 to 70 can be attributed to continued hydration of the bentonite.

data in Fig. 3 indicates that swelling was ongoing at the end of stage 2. However, based on the final 5 days of data from this stage, the rates of change were relatively small: 11.3 and 3.4 kPa/d for A1-A4 and A5-A8 respectively. The higher rate of change in the base of the sample relates to the aforementioned availability (or rather lack) of water. It is also noteworthy that, by the end of the stage, the variation in axial stress measured across each plane was very similar (0.69 MPa and 0.63 MPa for A1-A4 and A5-A8 respectively), see Table 4.
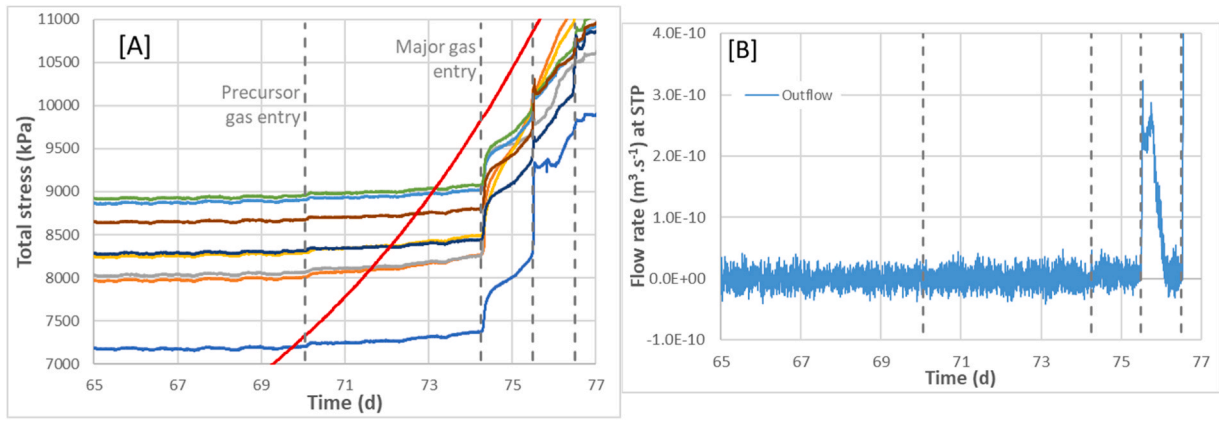
The development of radial stress evolves in a similar manner to that of the axial stress. When the clay was exposed to water, radial stresses also rapidly increased, Fig. 4, approaching a well-defined asymptote by the end of the stage. Inspection of the data shows some variability, even

across the same plane of measurement, such as the difference in values between sensors R9 to R12, or R13 to R16. Analysis of the data in Table 4, indicates larger variations in pressure exist as the distance to the points of measurement increase from the three sources of hydration. This results in some degree of heterogeneity in the resultant stress field at the end of stage 2, probably linked to a combination of incomplete homogenisation of the bentonite and subtle variations in the micro-structure of the sample. The data in Fig. 5 indicates that average radial stress does not change along the length of the sample. This suggests that friction between the sample and vessel wall is likely to play a small (if any) role in the development of the stress on the scale of the experiment. The difference between axial stress at the top and bottom of the sample (Fig. 3) therefore relates to the availability of water (which is less at the base of the sample) suggesting incomplete homogenisation at this region of the sample. However, the length of time required to fully homogenise bentonite is unclear and remains a research priority within the European Community. As time was limited and the average values of radial stress, Fig. 5, were relatively similar across each measurement, the sample was deemed ready for gas testing.
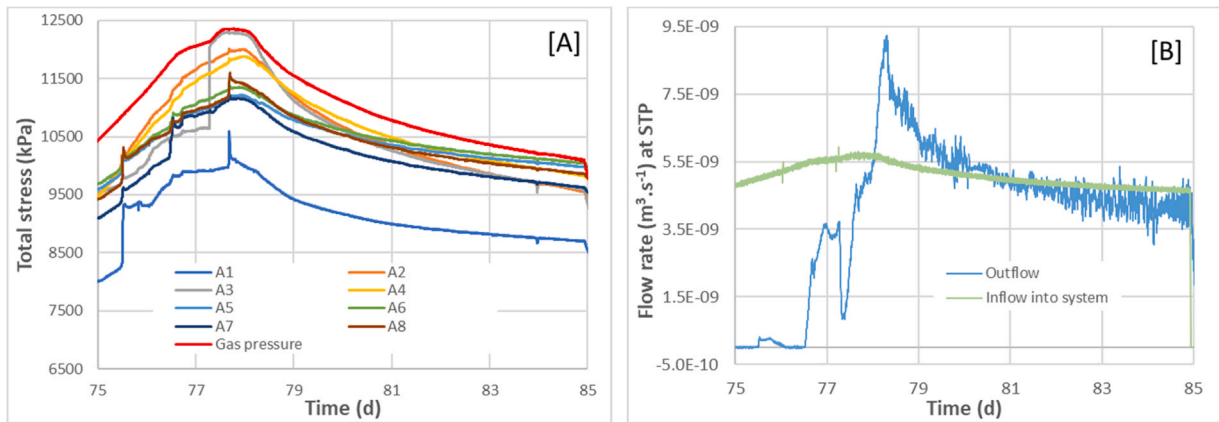
Following a brief period of further equilibration, gas testing (stage 4) began on day 28.4, with the injection pump set at a constant displacement rate of 180 µl/h. Gas pressure gradually increased for the following 49.4 days, reaching a peak value of 12.36 MPa at day 77.8, see Fig. 6. This was followed by a spontaneous negative pressure transient leading to a quasi-steady state around day 84.9. At this point, the injection pump was stopped, test stage 5, and the pressure allowed to slowly decay. Gas pressure continued to decline until the test was stopped at day 117. Closer inspection of the axial stress data, see Fig. 7[A], suggests a small gas entry (i.e., onset of flow into the clay) event occurred around day 70.1, shortly after gas pressure exceeded the lowest value of axial stress. However, inspection of the outflow data, Fig. 7[B], shows no obvious sign of discharge. In the absence of a suitable sink, gas pressure therefore continued to increase, finally resulting in a major gas entry event around day 74.3 at a gas pressure of around 9.84 MPa. In the intervening time between the precursor and major entry events, the rate of change in all stress traces began to increase, providing clear evidence of a hydrodynamic effect caused by the coupling between gas pressure and axial stress.

Further examination of the outflow data following the major gas entry event at day 74.3, Fig. 7[B], suggests a very small increase in outflow occurred around this time, possibly caused by compaction of the clay following major gas entry. However, gas breakthrough did not occur until day 75.5, from which it can be inferred that it took 1.2 days for sufficient pathways to develop and locate the backpressure filter. At this point, outflow rapidly increased and was associated with a series of spontaneous changes in the stress field, Fig. 7[A]. However, the initial development of permeability was short-lived, as conductive pathways began to spontaneously close and outflow quickly decreased. From day 76.1 to 76.5, outflow reduced to pre-major breakthrough levels and was accompanied by further increases in gas pressure and stresses within the sample, as gas pathways developed to reconnect with the backpressure filter. Towards the right margin of Fig. 7[B], outflow from the sample spontaneously increased for a second time at day 76.5 and was again associated with complex changes in the stress field.
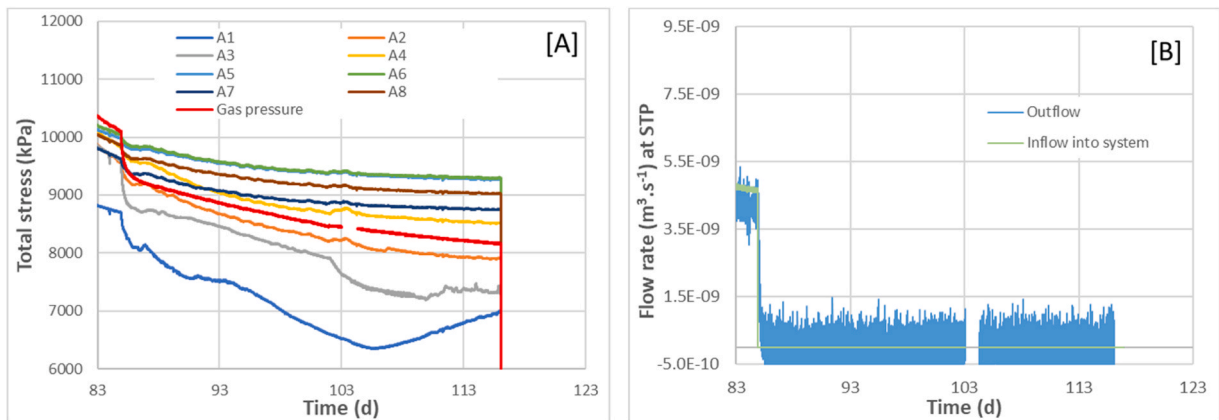
Fig. 8 shows the evolution of axial stress in response to the development of flow out of the sample. Gradual and abrupt changes in gas pressure and stress were observed that are interpreted as linking to the development of flow paths within the sample. This behaviour is consistent to previous experimental observations (e.g.,[15] and[17]). Following major gas breakthrough outflow, stress and gas pressure were highly coupled. In general, gas pressure remained slightly above that of axial stress, suggesting some degree of pressure drop along gas pathways. However, the orientation of the pathways to the direction of stress measurement strongly impacts the measured value of stress. Therefore, a detailed analysis of the stress response (axial and radial) is required and will be undertaken at a future date.

Fig. 7. Data from part of stage 4 of test FPR-21–004 with dotted lines denoting significant events. [A] expanded view of gas pressure and axial stress data showing precursor gas entry around day 70.1 followed by major gas entry at day 74.3. Line colours are the same as those on Fig. 6. [B] shows time averaged outflow data under experimental conditions with major gas outflow occurring at day 75.5.

Fig. 8. Data from part of stage 4 of test FPR-21–004. [A] development of axial stress and [B] evolution of inflow and outflow data at STP, from day 75–85. Combined, the data illustrates the complex coupling between development of flow and accompanying changes in stress within the bentonite.

Fig. 9. Shut-in, test stage 5, for sample FPR-21–004. [A] change in gas pressure and axial stress and [B] evolution of outflow (at STP) following the cessation of pumping at day 84.9 (the missing data at day 103 was caused by a problem with the data logger).

While the peak gas pressure response was more rounded in shape compared to the that of outflow, peak gas pressure occurred prior to peak outflow. This suggests a degree of time-dependent behaviour in the development of gas pathways and thus permeability within the sample. However, by the end of the test stage at day 84.9, Fig. 8[B], inflow and outflow were converging, signifying the test was approaching a near steady state condition. However, close examination of the data shows

small discrepancy between inflow and outflow data at day 84.9. As the system was not in true steady-state, it is not possible to identify the true origin of this discrepancy, but might stem from a small background leak.

As soon as the injection pump was stopped, gas pressure, axial stress and outflow from the sample rapidly decreased, Fig. 9. For the first time, gas pressure dropped below axial stresses A2 and A5 through A8, suggesting depressurisation of some pathways and trapping of residual gas
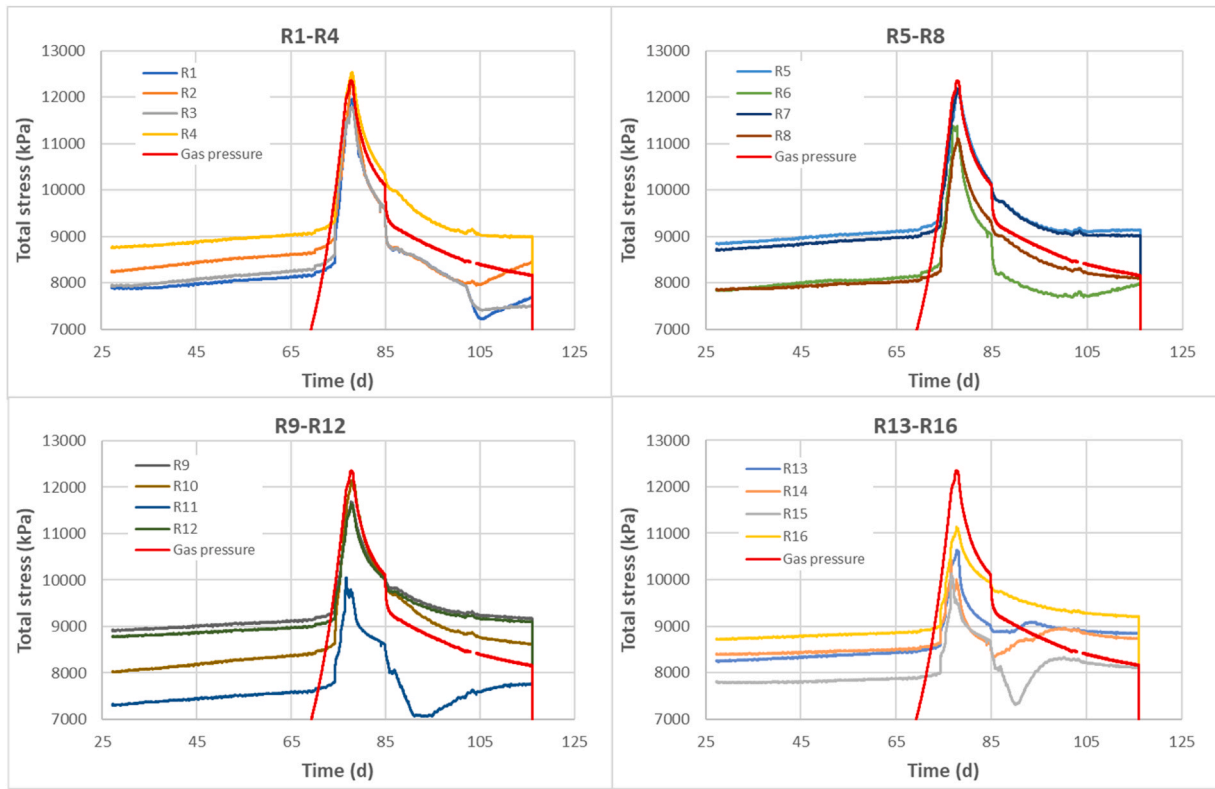
Fig. 10. Radial stress data for FPR-21–004. Radial stresses R13 through R16 register the lowest values as these sensors were located below the injection filter.
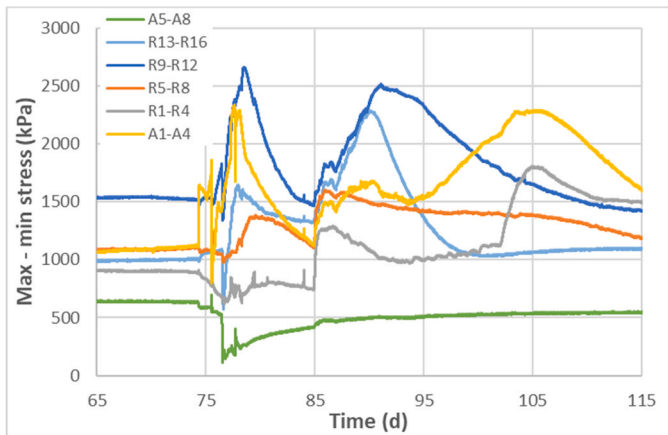

Fig. 11. Difference between maximum and minimum stress at each axial and radial plane of measurement plotted as a function of time.

Fig. 12. Average stress at each plane of measurement along the axis of sample FPR-21–004.

in others. From day 87, a more gradual decline in gas pressure and axial stress was observed. By the end of the stage, gas pressure was over 1.0 MPa lower than axial stress at sensors A5 and A6. Examination of Fig. 9 indicates the variation in total stress increases as the shut-in stage progresses. This is likely caused by the localised closure of gas pathways, resulting in the entrapment of gas within the sample, perturbing the stress field.

The disconnect between outflow and changes in axial stress and gas pressure suggests complex patterns of flow drainage, which spatially evolved within the clay. This indicates that pathway closure can be rapid, as in the early stages of the shut-in response, or slow, as illustrated by the subsequent gradual decline in axial stresses and gas pressure. The early, rapid, pathway closure may be driven by the elastic (compressibility) of the material and the subsequent gradual response by the slow
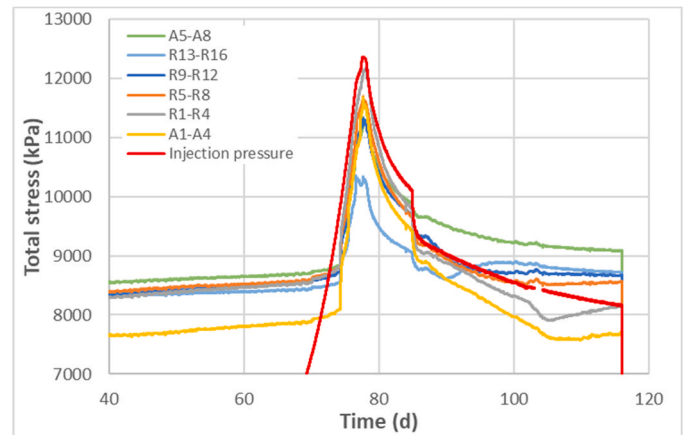
diffusion and egress of gas trapped along now partially sealed pathways.

Fig. 10 shows the evolution of radial stress during gas injection, test stages 4 and 5. These sensors showed qualitatively similar behaviour to that previously discussed for axial stress. Considerable variations in stress values were observed across each plane, Fig. 11, ranging from 140 kPa to 2650 kPa. The data clearly shows the evolutionary and complex nature of the stress field induced during advective gas flow and is likely linked to the localised internal development of gas pathways within the clay.

A plot of average stress for each plane of measurement, Fig. 12, shows that once major gas entry occurred, stress increased fairly consistently throughout the sample, with the exception of R13-R16. Here peak stress was substantially lower compared to all other arrays, suggesting fewer pathways propagated towards the top of the sample. In
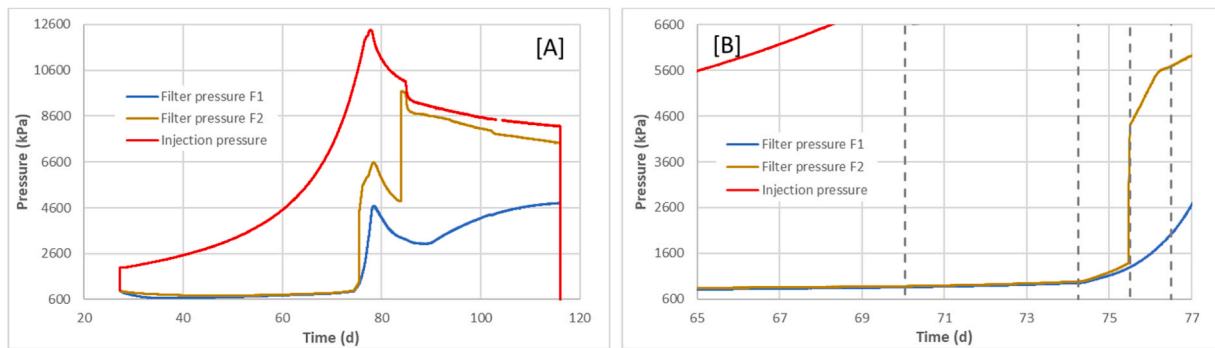
Fig. 13. [A] pore pressure development in filters F1 and F2 during test FPR-21–004. [B] expanded data from day 65 to day 77 showing the filter response during initial gas entry, major gas entry, initial gas breakthrough and major gas breakthrough respectively from left to right.

contrast, during the major gas entry and breakthrough events, average stress values for A1-A4 were similar to those in array A5-A8, suggesting some pathways must have been horizontally orientated across the vertical axis of the sample. The highest stress values occurred in array R1-R4, closest to the backpressure filter, indicating that (i) the gas pressure gradient induced presumably small pathways and (ii) most of the pressure drop between the gas phase and the water within the backpressure filter occurred in a narrow zone close, or at, the edge of the sample.

The evolution in pore pressure at filters F1 and F2, within sample FPR-21–004, is shown in Figure 13[A]. Following the cessation of hydration at day 27.2, a gradual decrease in pressure was observed, illustrating that the sample was not in full hydraulic equilibrium at the onset of gas testing. As hydration continued from the backpressure filter, a gradual increase in water pressure was seen from around day 38 and 49 in filters F1 and F2 respectively. Figure 13[B] shows the development of pore pressure during gas entry and subsequent breakthrough events. As major gas entry occurred at day 74.3, both filters showed an increase in pressure, probably related to a hydrodynamic effect during the displacement and compaction of the clay at gas entry. As injection gas breakthrough occurred at day 75.5, filter F2 showed a rapid increase in pressure, most likely due to the arrival of gas at the filter. Gas pressure peaked at 6.64 MPa and then began to gradually decrease. A second breakthrough event in the same filter, occurred at day 84 when pressure rapidly increased. Filter pressure then appeared correlated to the gas pressure with an offset of around 0.7 MPa by the end of stage 5. This data also demonstrates that the pressure drop along the connected gas pathways, from the injection point to the filter, was relatively small.

In contrast, the development of pressure within filter F1 showed no abrupt changes in pressure as with filter F2. This suggests that filter F1 was likely recording local hydrodynamic changes in porewater pressure due to displacement and localised compaction of the clay as gas pathways formed. However, the increase in pressure of filter F1 from around day 87, as gas pressure declined, might be linked to the slow discharge of gas into the filter as the pathways began to drain.

3. Enriched multi-phase modelling approaches

Three different numerical approaches have been adopted by BGR/ UFZ, LBNL and CIMNE-UPC/Andra (see also Appendix A for details about their key similarities and differences). These three strategies are based on the general theory of multi-phase flow modelling and are combined with additional features to describe some of the key aspects observed in gas-laboratory tests that distinguish clay-rich media from other rock-types (e.g., deformation of the porous media, creation of dilatant preferential pathways that open and eventually self-seal). Indeed, the bentonite sample is modelled as a deformable porous medium that behaves as either an elastic (LBNL, CIMNE-UPC/Andra) or an elasto-plastic (BGR/UFZ) solid. Intrinsic permeability is treated as a function of other properties during the gas injection test, representing

the dilatant pathways. In particular, intrinsic permeability is assumed to depend either on the strain tensor (BGR/UFZ), on the effective minimum compressive stress (LBNL) or on the embedded fractures aperture and spacing (CIMNE-UPC/Andra). The water retention curve is also assumed to be a function of embedded fractures aperture and spacing in the model developed by CIMNE-UPC/Andra.

3.1. Model developed by BGR/UFZ

3.1.1. Conceptual model

The model expands upon the work performed by BGR/UFZ within the Task A DECOVALEX-2019 (D-2019), where the team developed a hydro-mechanical model for migration of gas through a low-permeable linear elastic geomaterial that included a pressure-dependent intrinsic permeability. Indeed, for the current phase of DECOVALEX-2023, BGR/ UFZ developed a fully coupled, hydro-mechanical model based on multiphase flow theory,[23] whose key features are:

- **Constitutive relations for the hydraulic behaviour**: the Mualem model is adopted for the description of the relative permeabilities of gas and water whereas the relationship between water saturation and capillary pressure is based on the van Genuchten formulation,[34].
- **Constitutive relations for the mechanical behaviour**: bentonite is assumed to behave as an elasto-plastic porous medium. Hooke's law is assumed to describe the stress-strain relationship in the elastic regime of the material whereas the Drucker-Prager failure criterion is assumed to describe the plastic deformation (perfect plasticity with non-associated flow). This is enhanced with a tension cut-off parameter to limit the load carrying capacity of the model near the tensile region.
- **Hydro-mechanical coupling**: Biot's theory[35] is assumed to describe the hydro-mechanical coupling. That is, the effective stress tensor $\boldsymbol{\sigma}'$ (Pa) is calculated from the pore pressure **p** and the total stress tensor $\boldsymbol{\sigma}$ as

$$\boldsymbol{\sigma}' = \boldsymbol{\sigma} - \alpha \mathbf{p} \tag{1}$$

(where α (-) is the Biot's coefficient) and used to define the linear momentum balance equation of the porous medium

$$\nabla\left[\boldsymbol{\sigma}' - \alpha\left(p_g - S_w p_c\right)\mathbf{I}\right] + \rho\boldsymbol{g} = 0 \tag{2}$$

where p_g (Pa) is the gas pressure, S_w (-) is the water saturation, p_c (Pa) is the capillary pressure, **I** is the identity tensor, ρ (kg/m^3) is the total density and $\boldsymbol{g}$ (m/s^2) is the gravitational acceleration.

Material heterogeneity is included in the model by means of the gas entry pressure and Young's modulus, which are described with a heterogeneous distribution. Both can be derived from a non-uniform distribution of the dry density, which has been observed in similar experiments.[36] The approach does not attempt to represent the scale of
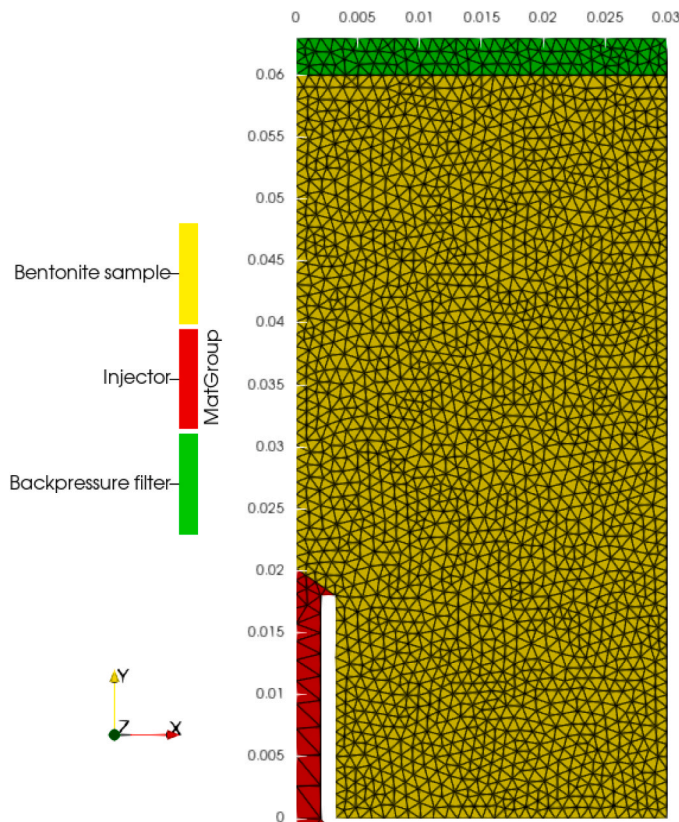
Fig. 14. Axisymmetric mesh (with 2716 triangular elements and 1448 nodes) used by BGR/UFZ to simulate the test.

the microstructure in finite elements. Rather, it tries to simulate a statistical reproduction of measured value ranges by means of variance and mean value. Since there is not a detailed analysis of the dry density of the bentonite sample, measured stresses and pressures are used for the implementation of the heterogeneity. The variance of the Young's modulus is derived from the stress measurements and the gas entry pressure is derived from the observed gas entry into the bentonite. The stress measurements at the beginning of the experiment (Fig. 3) are approximately between 7 MPa and 8.5 MPa. Assuming a linear relationship between measured stress and Young's modulus, a standard deviation of 0.27 GPa can be calculated. The mean value for the Young's modulus is 3.5 GPa. A Gaussian normal distribution is assumed for the distribution. For the distribution of the gas entry pressures, the measured gas pressures are analysed at which gas first enters the bentonite and at which the main part of gas enters. The first inflow is measured at a gas pressure of 7.3 MPa, while the main inflow occurs at 9.8 MPa (Fig. 7). From this, a mean value for the gas entry pressure of approx. 10 MPa and a standard deviation of 2 MPa are determined.

Dilatant pathways are modelled by including the strain-dependent intrinsic permeability relationship developed in[37].

$$\mathbf{k} = f(\varepsilon_{vol})e^{b_1\bar{\varepsilon}^p}\mathbf{k}_0 \qquad (3)$$

where

$$f(\varepsilon_{vol}) = \begin{cases} 10^{b_2\varepsilon_{vol}}, \varepsilon_{vol} \leq 0(\&\text{compaction}) \\ 10^{b_3\varepsilon_{vol}}, \varepsilon_{vol} > 0(\&\text{extension}) \end{cases} \qquad (4)$$

with ε_{vol} (-) being the volumetric strain, $\bar{\varepsilon}^p$ (-) being the equivalent plastic strain, $\mathbf{k}_0$ ($= 5 \times 10^{-20}$ m^2) being the initial intrinsic permeability tensor and b_1, b_2 and b_3 being empirical parameters controlling flow that need to be calibrated against experimental results. In particular, parameters b_2 and b_3 account for the increased flow velocities in the case of microfissuring, which might be observed when the gas pressure is still

lower than the minimum principal stress and tensile strength whereas b_1 is used to define a rapid increase of permeability once the tensile failure is reached. The volumetric strain is 0 at the beginning of the simulation. Maximum permeability increments triggered by volumetric strain and plastic strain are at a factor of 100 each. That is, a theoretical increase in intrinsic permeability of 10,000 can occur at high volumetric and plastic deformations. However, it should be noted that the model is only validated for small plastic deformations and only small deformations can be realistically calculated with the finite element method. The prescription of their values is difficult and the sensitivity analysis performed to simulate the test will be discussed in the following section. The higher permeability paths are triggered by the heterogeneous distribution of Young's modulus, which is expected to result in a non-uniform strain development. Its mean needs also to be empirically calibrated and details about the sensitivity analysis performed to simulate the test are also reported in Section 4.

3.1.2. Model geometry and numerical software

A finite element method (FEM) 2D model has been developed to analyse the test described in Section 2. The open-source software OpenGeoSys (OGS - version 5.8) has been used, see.[38] To simulate the test, a triangular 2D axisymmetric mesh has been used, see Fig. 14.

In this current phase of the DECOVALEX project, the injector (assumed rigid) has been explicitly modelled by means of the addition of a source term (whose value needs calibration against experimental measurements) that allows the simulation of the increasing pressure. It is defined by a high porosity ($= 0.5$) and a high permeability value ($= 1 \times 10^{-17}$ m^2). Relatively low values have been chosen here for the injector material, to reduce numerical issues at the boundary between the injector and the bentonite. However, in relation to the bentonite permeability, the intrinsic and relative permeability combined are around 10^{10} higher.

3.1.3. Initial and boundary conditions

The sample has been considered to be initially saturated (initial value of 97%) by assuming an initial capillary pressure of 2.0 MPa. First, a constant gas pressure of 3.0 MPa has been prescribed to account for a water pressure of 1 MPa (as dictated by the sorption equilibrium equation, see[39]). An initial compressive effective stress of 7.0 MPa (in each direction) has been defined to account for the swelling stress reached by the material during saturation.

No displacements are prescribed at the boundaries including the central borehole, see Fig. 14. Injection pressure is prescribed at the bottom of the injector material group whereas backpressure is prescribed at the upper boundary.

3.2. Model developed by LBNL

3.2.1. Conceptual model

This model builds upon LBNL's experience previously gained during Task A DECOVALEX-2019 (D-2019) since, as part of D-2019, LBNL developed and numerically applied two different approaches: a multiphase flow model (i) combined with additional hydro-mechanical features and (ii) coupled to a discrete fracture modelling approach.[40] Indeed, for the current phase of DECOVALEX-2023, LBNL enhanced their homogeneous continuum approach, which is based on the linking of the multiphase fluid flow simulator TOUGH2 with the commercial FLAC^{3D} geomechanical code thus enabling the simulation of processes characterised by strongly-coupled flow and geomechanics. Key features of this current enhanced continuum approach are:

- **Constitutive relations for the hydraulic behaviour**: as done by BGR/UFZ, the van Genuchten formulation is used to define the water retention curve. Relevant capillary pressure parameters for the bentonite are adopted from.[41] In this model, Corey model is adopted for the description of the relative permeabilities of gas and water.
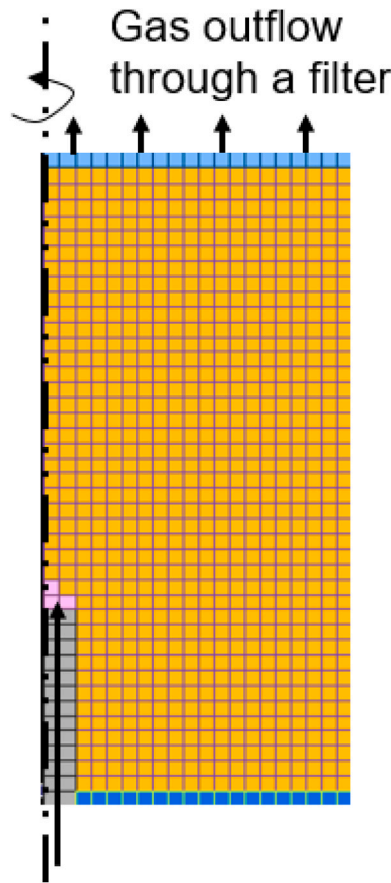
Fig. 15. Axisymmetric mesh (with roughly 900 elements, including element representing the injection filter and the injection chamber) used by LBNL.

- **Constitutive relations for the mechanical behaviour**: bentonite is assumed to behave as a linear elastic porous medium, with a volumetric swelling and a swelling stress that depends on the changes in water saturation ΔS_l according to

$$\Delta \boldsymbol{\sigma}'_{sw} = \mathbf{K} \Delta S_l \beta_{sw} \tag{5}$$

where $\boldsymbol{\sigma}'_{sw}$ (Pa) is the swelling stress, $\mathbf{K}$ (Pa) is the bulk modulus, S_l (-) is the liquid saturation and β_{sw} [-] is a calibrated moisture swelling coefficient ($\beta_{sw} = 0.02$ in D-2019 and decreased up to $\beta_{sw} = 0.015$ in D-2023 to better match the experimentally-observed stress increase), see[42] for more details.

- **Hydro-mechanical coupling**: in this model, the effective stress tensor $\boldsymbol{\sigma}'$ (Pa) responds to the maximum phase pressure p^ϕ in the pore, that can be either gas pressure (if gas partially saturated) or liquid pressure (if fully water saturated). That is,

$$\boldsymbol{\sigma}' = \boldsymbol{\sigma} - p^\phi \mathbf{I} \tag{6}$$

where again, $\boldsymbol{\sigma}'$ and $\boldsymbol{\sigma}$ are the effective and total stress tensors respectively, $\mathbf{I}$ is the identity tensor and the pore pressure p^ϕ is defined as

$$p^\phi = \max(p_l, p_g) \tag{7}$$

with p_l and p_g liquid and gas phase pressures respectively.

As in D-2019, this model assumes a fracture-like behaviour of the flow path. Hence, a stress dependent permeability function

$$k = k_{\text{matrix}} + \frac{b_h^3}{12a} \tag{8}$$

is again considered, where a [m] is the element width and b_h [m] is a

non-linear function of the effective minimum compressive stress that reads

$$b_h = \frac{b_{h0}}{1 + 9 \left(\frac{\sigma_n - P}{\sigma_{n,\text{ref}}} \right)} \tag{9}$$

with b_{h0} (m) being the (calibrated) maximum aperture for permeability, σ_n (Pa) the total stress normal to the fracture and $\sigma_{n,\text{ref}}$ (Pa) the adjusted reference stress normal to the fracture. In these simulations, the total normal stress to the fractures is taken as the minimum compressive stress. The aperture versus pressure relationship of Eq. (9) corresponds to the model described in[43] and its parameters need to be calibrated by matching pressure and outflow responses observed in the experiments, see Section 4 for more details. To be able to simulate the abrupt gas breakthrough response, the concept of a constant effective gas entry pressure has been adopted by LBNL. As done by BGR/UFZ, a heterogeneous gas entry pressure might be considered in future approaches, together with heterogeneous porosity and permeability fields.

3.2.2. Model geometry and numerical software

The simulator applied in this study is the TOUGH-FLAC code,[44] that combines the TOUGH2 multiphase flow simulator[45] with the commercial geomechanics code FLAC3D.[46] TOUGH2 enables the simulation of multiphase fluid flow and heat transport based on the integral finite difference method whereas FLAC3D is a finite-difference code that allows the representation of geomechanical features. Similar to other TOUGH-based geomechanical simulators, the two codes are sequentially coupled: in particular, fluid flow variables (such as pore pressure and saturation) calculated by TOUGH2 are transferred to FLAC3D, which then computes effective stresses and associated deformations, returning updated values for the stress-dependent permeability. The selection of small time-steps is important to find stable solutions of the hydraulic and mechanical response: a maximum time step of 1 day is here prescribed while smaller time-steps (e.g., 100 s) are automatically calculated by TOUGH2 for convergence in the multiphase flow calculations around the gas breakthrough. This is the main computational challenge that arose when running simulations: during abrupt changes in saturation and permeability (at the instant of gas breakthrough) time steps were reduced to very small values for convergence in the sequentially coupled hydro-mechanical solution process.

To simulate the test described in Section 2, a quadrilateral 2D axisymmetric mesh has been used, see Fig. 15. The use of an axisymmetric model allows to obtain simulation results within a reasonable time (on the order of 20 min) by employing relatively small number of elements and nodes, see Appendix A.3. However, it is inherently limited to the analysis with homogeneous material properties, thus meaning that heterogeneous properties and flow paths cannot be rigorously considered. To properly consider heterogeneous material properties, a full 3D model would be required.

As seen, the injector is explicitly modelled considering a representative volume of the injection chamber. For the simulations, gas is injected by prescribing its injection rate (in kg/s). This value needs to be calibrated by fitting the pressure increment in the injection chamber against the observed pressure increments.

3.2.3. Initial and boundary conditions

The sample and the injection chamber have been considered to be fully initially saturated (2 MPa water pressure). A backpressure of 1 MPa has been also assumed and an initial stress of 8.0 MPa has been defined. The sample is mechanically confined during the entire simulation: no displacements normal to the boundaries are prescribed. A no-flow condition has been assumed at the boundaries, except at the injection and outflow filters.
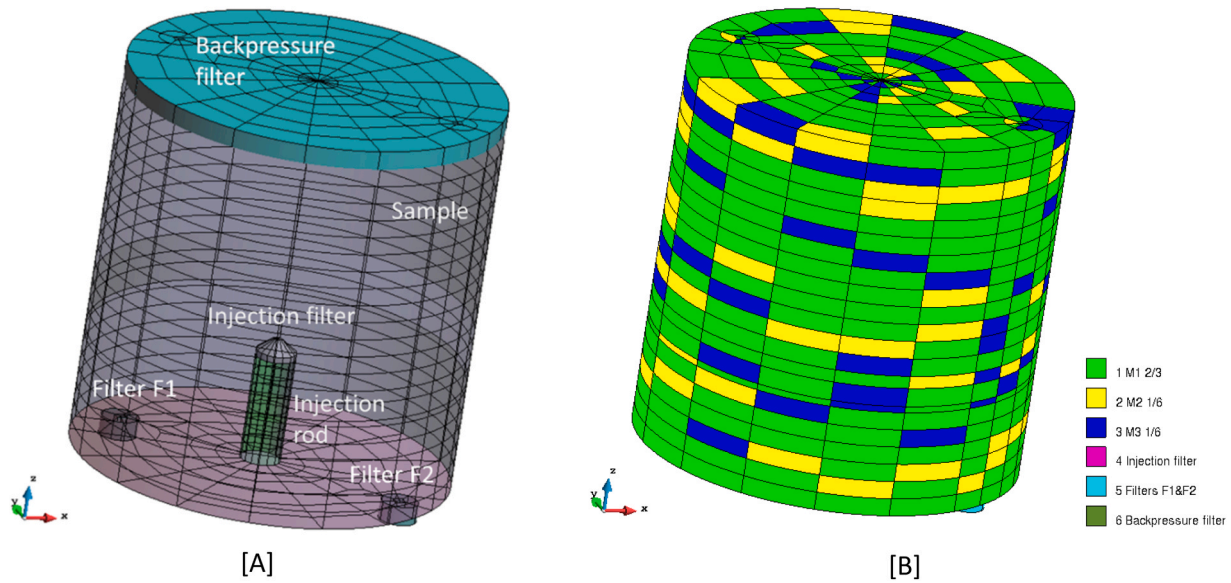
Fig. 16. 3D mesh (with 3430 elements and 3909 nodes) used by CIMNE-UPC/Andra to simulate the test: [A] shows the modelled sample mesh and the main component details and [B] shows the material heterogeneity (2/3–1/6–1/6 weighting).

3.3. Model developed by CIMNE-UPC/Andra

3.3.1. Conceptual model

This model is built on the work carried out by CIMNE-UPC/Andra within the previous phase of the DECOVALEX project, see,[26] where a coupled hydro-gas-mechanical 3D numerical model was developed assuming a heterogeneous initial permeability field and embedded fractures.[47] This approach is characterised by the following key features:

- **Constitutive relations for the hydraulic behaviour**: in the model developed by CIMNE-UPC/Andra, the retention curve is defined by the van Genuchten model. In this case, the retention curve may change with the opening of the embedded fractures as pore size controls the gas entry values, and fractures may represent large pores leading to a reduction of the gas entry value. Relative permeabilities are also assumed to be fracture-dependent to account for preferential paths. This is achieved by assuming that the relative permeability, which is a function of the effective degree of saturation, is decomposed into matrix and fracture terms, as discussed in the following paragraph.
- **Constitutive relations for the mechanical behaviour**: deformation is modelled assuming elasticity with net stress (fluid pressure as the maximum between gas and liquid). A dilatancy term (ψ angle) is added in the deviatoric component of the volumetric strains

$$\Delta \varepsilon_v = \frac{\Delta p^{'}}{K} - \frac{\Delta q}{3G} \tan\psi \tag{10}$$

$$\Delta \varepsilon_d = \frac{\Delta q}{3G} \tag{11}$$

where $p^{'}$ and q correspond to the net mean stress and deviatoric stress invariants, and K and G to the bulk and shear modulus, respectively (compression positive). As done by LBNL, net mean stress is defined as total stress minus Biot's coefficient times fluid pressure (maximum between gas and liquid pressures), see Eqs. (6) and (7)7.

- **Hydro-mechanical coupling**: in the proposed approach, it is assumed that the mechanical constitutive model and the permeability model are coupled but independent. That is, the mechanical behaviour is coupled to the hydraulic/gas because the volumetric strains cause changes in permeability, through changes in aperture.

To account for the preferential paths, a constitutive model based on an integrated embedded permeability is employed. The strategy is based on the decomposition of the intrinsic permeability into a matrix and a fracture intrinsic permeability

$$k_{\text{int}} = k_{\text{matrix}} + k_{\text{fracture}} \tag{12}$$

which undergo respective variation with porosity and aperture and read

$$k_{\text{matrix}} = \frac{k_0(1-\phi_0)^2}{\phi_0^3} \frac{\phi^3}{(1-\phi)^2} \tag{13}$$

$$k_{\text{fracture}} = \frac{b^3}{12a} \tag{14}$$

where k_0 (m^2) is the initial permeability (randomly distributed along the material); ϕ_0 (=0.44) is the initial porosity; ϕ (-) is the current porosity value, changing in space and time during the test; a (m) refers to the internal associated width for each fracture (which is equivalent to the assumed spacing between fractures) and b (m) is the aperture of the fractures. This value depends on the strain ε (-) and on the initial strain ε_0 (-) and may be computed as

$$b = b_0 + \langle \varepsilon - \varepsilon_0 \rangle a \le b_{\max} \tag{15}$$

with b_0 (m) and $b_{\max}$ (m) being the initial and maximum aperture of the fractures. Liquid- and gas-phase permeabilities are also decomposed into matrix and discontinuities or fractures terms. These read

$$k_{\text{liquid}} = \left(S_{\text{eff, liquid}}\right)^{m_{\text{liquid}}} \left(k_{\text{matrix}} + k_{\text{fractures}}\right) \tag{16}$$

$$k_{\text{gas}} = \left(S_{\text{eff, gas}}\right)^{n_{\text{gas}}^{\text{matrix}}} k_{\text{matrix}} + \left(S_{\text{eff, gas}}\right)^{n_{\text{gas}}^{\text{fractures}}} k_{\text{fractures}} \tag{17}$$

respectively, with $S_{\text{eff, liquid/gas}}$ (-) being the saturation degree for liquid or gas and $n_{\text{liquid/gas}}^{\text{matrix/fractures}}$ (-) being a power for each case state (i.e., for liquid or gas state, and for matrix or fractures media). As previously stated, liquid and gas relative permeabilities are defined by the effective saturation degree of liquid and gas respectively. Hence,

$$k_{\text{r,liquid/gas}} = \left(S_{\text{eff, liquid/gas}}\right)^{n_{\text{liquid/gas}}} = \left(\frac{S_{\text{liquid/gas}} - S_{\text{liquid/gas}}^{\min}}{S_{\text{liquid/gas}}^{\max} - S_{\text{liquid/gas}}^{\min}}\right)^{n_{\text{liquid/gas}}} \tag{18}$$
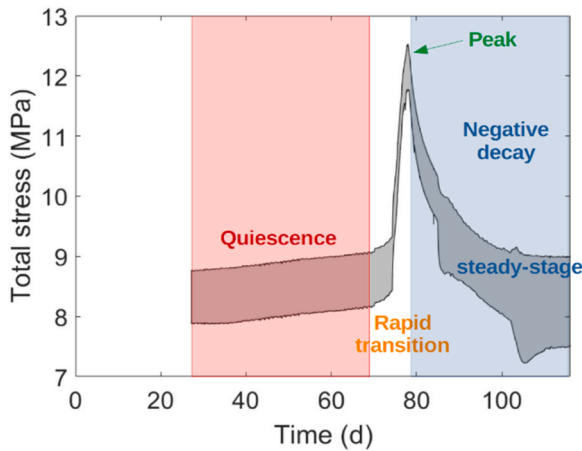
Fig. 17. Key components that characterise experimental stresses.

3.3.2. Model geometry and numerical software

The computer software CODE_BRIGHT[48] has been used to carry out the numerical simulations. CODE_BRIGHT is a finite element-based code developed at the Universitat Politècnica de Catalunya - BarcelonaTech (DECA-UPC) and the International Centre for Numerical Methods in Engineering (CIMNE).

To simulate the test of Section 2, a 3D hexahedral mesh has been developed, see Fig. 16. As seen, the 3 mm-thick base (F1 and F2) and backpressure filters have been considered. The injector has been explicitly modelled, assuming all relevant components (i.e., injection rod and injection filter tip), Fig. 16[A]. Additional global features of the injection/pumping system device (i.e., interface vessel, pipework, etc.) have not been considered but they have been represented through an equivalent volume factor applied to the injection filter. A detailed sensitivity analysis regarding the volume of the injector has been performed. As in previous Task A D-2019, calculations have been performed by considering a heterogeneous medium, where three different sample zones have been assumed to be randomly distributed, see Fig. 16 [B]. This produces heterogeneity of permeability and the retention curve. It is worth noting that mesh size is always a numerical challenge when modelling hydro-mechanical process and thus, the choice of the mesh involved a compromise between simplicity on the one hand and the capability of representing heterogeneity on the other.[49]
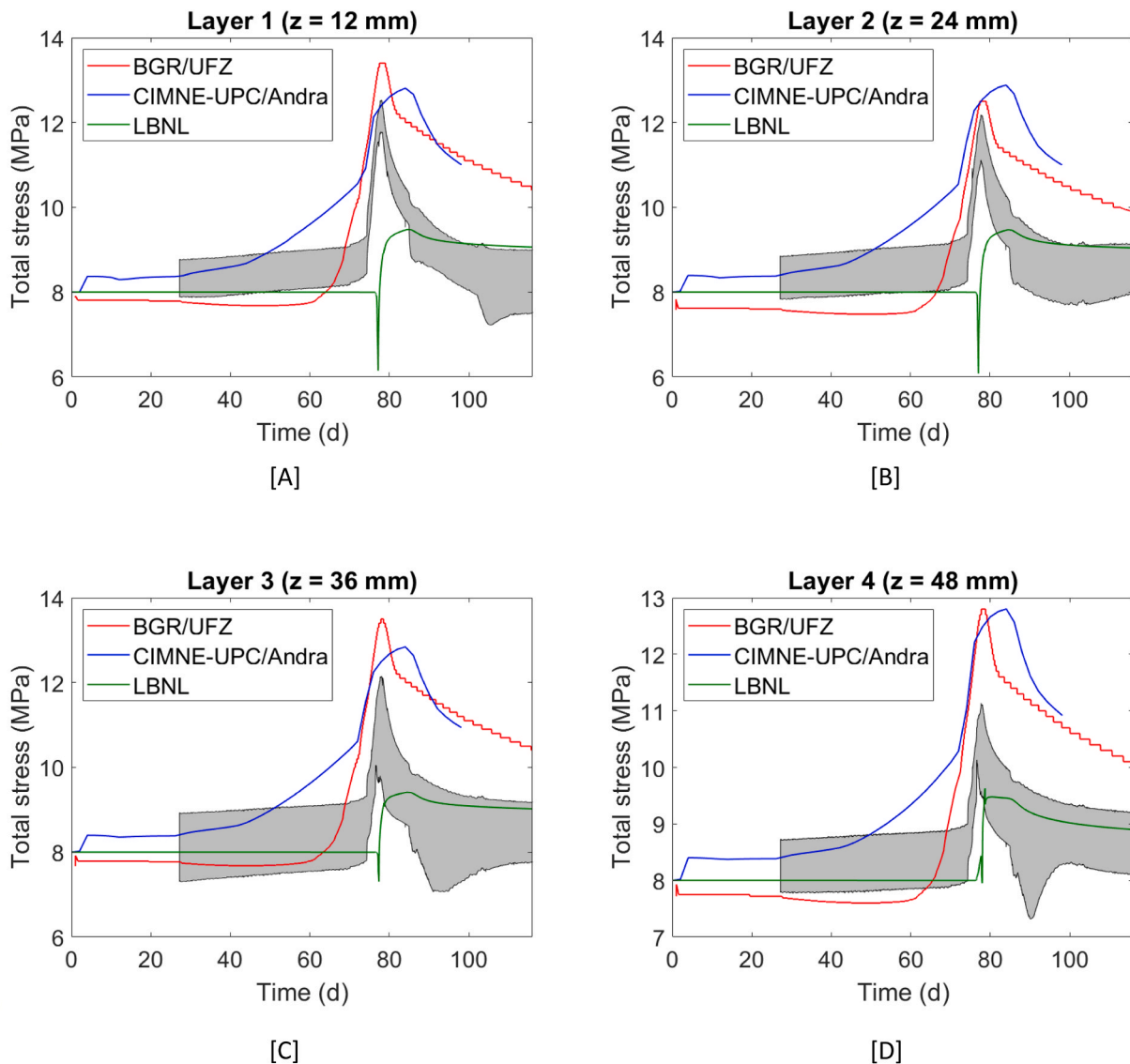

Fig. 18. Radial stresses obtained at each layer with the three numerical models. Grey zones represent experimental radial stresses.
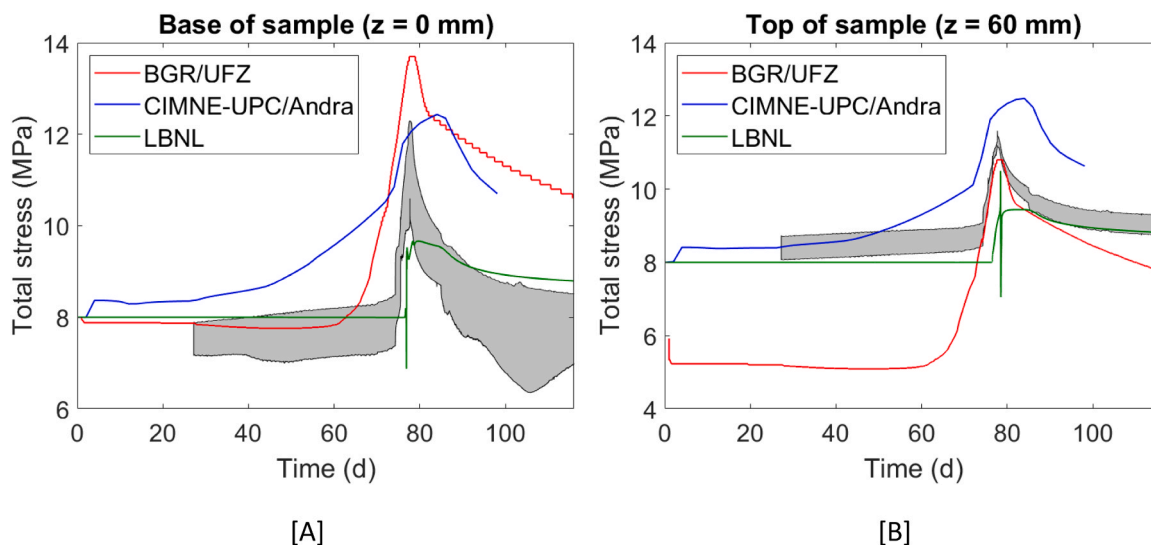
Fig. 19. Axial stresses obtained at both the base and the top of the sample with the three numerical models. Grey zones represent experimental axial stresses.
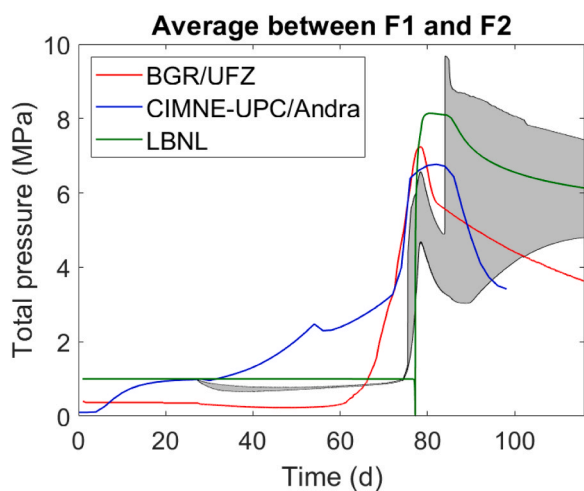

Fig. 20. Average pore pressure obtained with the three numerical models plotted against the whole range of experimental pore pressure.

3.3.3. Initial and boundary conditions

The sample has been considered to be initially water saturated. First, no initial stress was considered. After experimental dataset was released, an initial stress of 8 MPa has been assumed, corresponding to the swelling stress reached by the material during saturation. Boundary conditions have been prescribed so that they reflect the constant volume boundary test features. A no displacement condition (in any condition) is assumed at all the boundaries. This includes the sample-injection rod and filter contact. Once experimental results were released, refined boundary conditions (a refined injected gas flow ramp) have been considered, thus improving the numerical curves.

4. Results

The capabilities of the three numerical models (BGR/UFZ, LBNL and CIMNE-UPC/Andra) have been assessed by comparing the simulated results against the experimental ones obtained from the laboratory.

In particular, the following time histories were specified to be reported and are the key features of the comparison exercise:

1. Radial stresses curves in the 16 sensors (from R1 to R16).
2. Axial stresses in the 8 sensors (from A1 to A8).

3. Pore pressures in the 2 filters (F1 and F2).
4. Gas saturation profiles in the 24 sensors (from R1 to R16 and from A1 to A8)
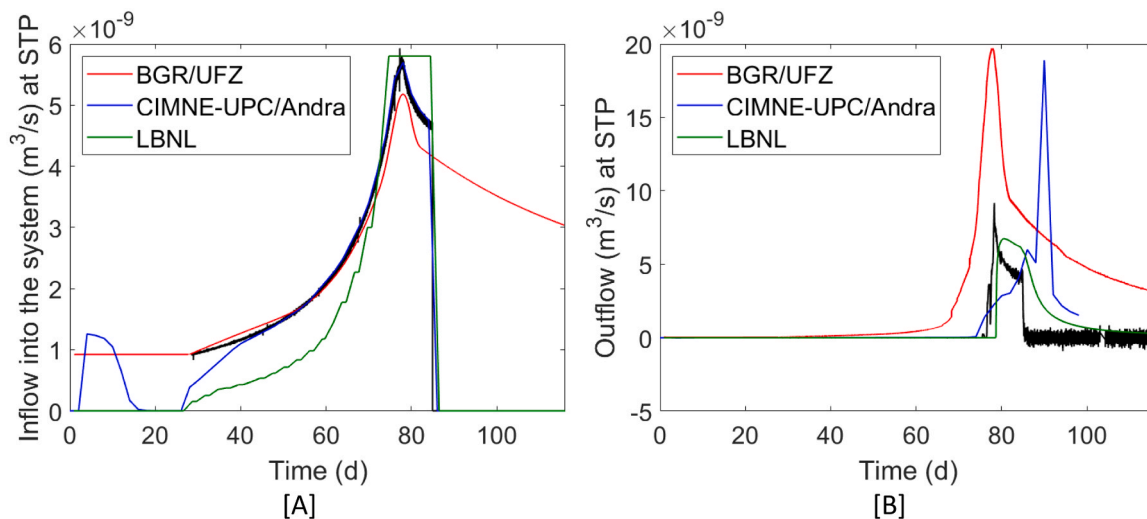5. Inflow into the system and outflow curves (at STP).

However, the teams were not asked to explicitly include the behaviour of the sensors used to measure changes in the stress within the bentonite sample. This has no bearing on the validity of the model outputs as sensor deformations were on the micron-scale (orders of magnitude below the models' scales). Some teams did include the representation of the injection system to improve model predictions.

A visual inspection of the experimental data (see Fig. 17) indicates that experimental radial and axial stresses can be summarised by four key components: (i) a quiescence phase, followed by (ii) the gas breakthrough, which leads to a (iii) peak value, which is then followed by (iv) a negative decay. Radial and axial stress results are shown in Fig. 18 and Fig. 19 respectively. As seen:

- **Quiescence phase**: all teams obtain good initial values.
- **Rapid transition phase**: reasonable responses are obtained after the modelling work performed during the study. However, some teams still predict a too-smooth response. Other key specific features (such as the breakthrough timing) still require a better representation. Indeed, the rapid stress increment is in general earlier modelled than experimentally observed.
- **Peak values**: they are in general reasonably-well captured. Maximum radial stress differences are observed at 48 mm from the base of the sample, where numerical peak values of 12.8 MPa are predicted by both BGR/UFZ and CIMNE-UPC/Andra, whereas experimental values are about 11 MPa (15% overprediction).
- **Negative decay**: models are capable of giving a reasonable representation of the negative decay. Some simulations should have been run for a little longer in order to analyse whether the steady-stage phase is finally captured.

Similarly, as with stresses, a visual inspection of the pore pressure data (Fig. 20) indicates that:

- **Quiescence phase**: some teams obtain good initial values, although others underpredict the initial stage.
- **Rapid transition phase**: in general, this remains a difficult experimental feature to capture. In some models, the response is too slow and the breakthrough is captured at earlier times than seen in the

Fig. 21. Flow curves at STP obtained with the model developed by CIMNE-UPC/Andra plotted against the experimental data (shown in black): [A] inflow into the injection system and [B] outflow.

experiment. This is most likely a numerical diffusion effect and necessary to get gas into the sample.

- **Peak values**: reasonably good peak values are obtained with the three models.
- **Negative decay**: the post-peak shape trend is well defined by all models. Again, the steady-stage phase is not numerically observed, as simulations have not run for sufficient time.

Inflow and outflow curves were also analysed. As seen in Fig. 21[A], some modelling teams used the experimental inflow as a boundary condition whereas others modelled the change in volume of gas based on the injection pump rate to determine the pressure from the ideal gas law. Thus, the analysis of the inflow modelling results makes it difficult to carry out a direct comparison. Fig. 21[B] shows the outflow results. The model developed by LBNL is capable of obtaining good fits with respect to both the abrupt increase in fluid flow and its timing. Other curves either show an earlier (BGR/UFZ) or a later (CIMNE-UPC/Andra) peak, whose value is overpredicted (almost a factor of 2 was observed). The observed shape of the post-breakthrough curve, which shows a shut-in behaviour and is directly linked to the stress state, is poorly reflected by all the models. This suggests a better understanding or representation of the hydro-mechanical coupling is still required.

As a summary, although the numerical approaches are not able to describe the full complexity of the physical processes, they are capable of matching key aspects of the evolution (e.g., peak values, breakthrough-timings, decay). The fact that some of the requested outputs are well represented without necessarily obtaining a good match to the entire dataset suggests that some of the underlying conceptual models are more/less sensitive to the individual couplings that appear in the system, and therefore that different models may be better/worse at representing selected aspects of the system evolution.

It is also worth noting that these numerical fits were obtained after a calibration process. Indeed, the adjustment of model parameters (see Appendix A) is needed and detailed sensitivity analysis are required. Their determination is extremely cumbersome (with no guarantee of uniqueness) since although each parameter primarily controls a particular effect with respect to the global response, all of them are correlated due to the very pronounced coupling between the hydraulic and mechanical response. These calibrated models lead to some calculated properties, such as gas saturations, being beyond physically reasonable values, suggesting the physical description of the system remains incomplete. Indeed, as seen in Fig. 22, some high gas saturation profiles are obtained by some models. As also seen, BGR/UFZ saturation profiles

are nearly constant throughout the simulation. This limitation is due to the fact that this model assumes that the pore fluid in the bentonite is located in the intra-aggregated pore spaces and therefore, it does not change much during the gas flow experiment. Indeed, the stochastic distribution of the gas entry pressure (see Section 3.1) is the responsible mechanism for the variability of the saturation in the bentonite.

The shown time series data are obtained in single points (at the sensors) and thus, categorical conclusions cannot be drawn. That said, post-test measurements yielded no measurable gas saturations within the sample as a whole. Therefore, high gas saturation profiles suggest that either the model capillary relationship governing desaturation is incorrect or too many pathways (with too high permeability) are present in the model.

5. Discussion

This paper presents a summary of a new gas injection test undertaken at BGS and the subsequent work performed in Task B of the current phase of DECOVALEX (DECOVALEX-2023) in which 4 teams have developed hydro-mechanical approaches for the modelling and representation of dilatant-controlled advective gas flow through very low-permeability materials. Validation against a one-dimensional gas test subjected to a constant volume boundary condition was performed by three of the teams. The experimental data from this gas injection test exhibits a combination of deterministic (e.g., breakthrough after a period of increasing gas pressure, bulk gas flow through a main emergent pathway) and stochastic (e.g., precise timing of the gas breakthrough, associated gas pathways) behaviours. It is therefore important for any analysis to distinguish between the key experimental features reproducible across all experiments and those that only occur in specific experiments.

This study allowed teams to test initial models and codes against a new dataset to verify the robustness of their predictions and thereafter enhance them in order to include the main deterministic features observed in these gas injection tests. To this end, other high-quality experimental datasets would be useful to help build additional confidence in the understanding of the key processes governing gas flow, the continued development and verification of numerical models, and the representation of these complex processes across different repository scales.

BGR/UFZ developed a hydro-mechanical model that included a pressure-dependent intrinsic permeability and an elasto-plastic heterogeneous porous medium. It is able to correctly capture initial and peak
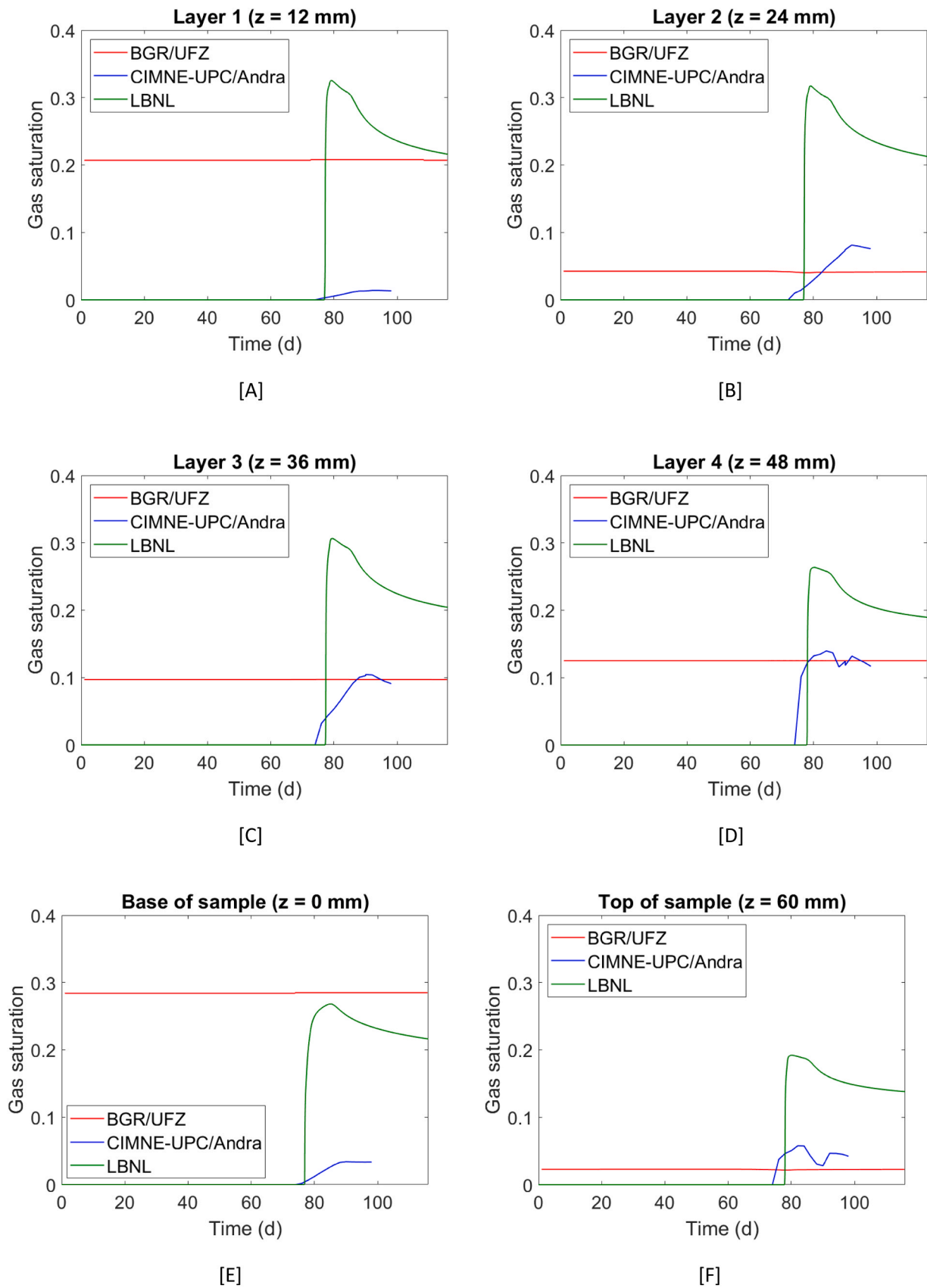
Fig. 22. Average gas saturation profiles at each layer, at the base and at the top of the sample obtained with the three numerical models.
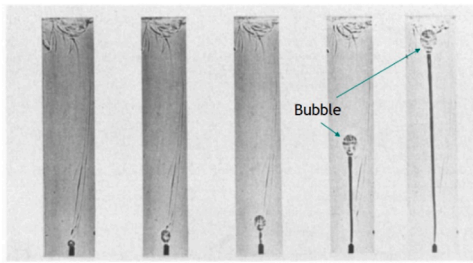
Fig. 24. Buoyant rising of a less viscous fluid within a more viscous fluid. Image is taken from [B.4].

stress values. However, the rapid transition phase seen at breakthrough is still too smoothly and too early predicted (Figs. 18 and 19). In terms of stresses, a similar behaviour is obtained when CIMNE-UPC/Andra's approach - a coupled hydro-gas-mechanical 3D numerical model that assumes a heterogeneous initial permeability field and embedded fractures - is employed. In terms of outflows, an earlier (BGR/UFZ) and a later (CIMNE-UPC/Andra) peak are obtained. LBNL applied a continuum approach, with a direct relation between permeability and least principal effective stress, that models dilatant permeability increase once the local fluid pressure approaches the least principal stress, i.e. the least principal effective stress approaches zero. This approach along with a gas entry pressure that is scaled with the dilation-induced permeability can be used to simulate the macroscopic gas flow behaviour (Figs. 18 and 19), although the model is not fine enough to capture microscopic dilatancy and heterogeneous gas channelling. The observed shape of the post-breakthrough curve, which shows a shut-in behaviour and is directly linked to the stress state, is poorly reflected by all the models thus suggesting a better understanding or representation of the hydro-mechanical coupling is still required. New conceptual models may therefore need to be developed to explain this complexity (Appendix B). However, their development is still in a very preliminary phase and at the current stage of the work, they are not able to reproduce the experiments. Thus, from a pragmatic perspective, enhanced flow models remain the only viable tool to represent these systems at this time.

In summary, this study illustrates further analyses are needed for a better understanding before models can be used, with confidence, as a predictive tool to assess advective gas movement:

- **Parameter calibration and model constraints**: developed models need calibration of fitted parameters. This poses a computational challenge as a large number of simulations are required. In addition, their adjustment is a complex task: indeed, although it is possible to evaluate the main effect of a single parameter on the global response, several parameter correlations exist due to the complex model couplings. A great effort from the modelling teams has been made to tackle this issue and detailed sensitivity analysis have been carried out to characterise the one-dimensional gas injection test. However, their extrapolation to other tests can be difficult. This was already observed in Task A D-2019,[21] where different parameter values for the 1D and the 3D tests were sometimes arbitrarily prescribed. Thus, more numerical analyses and a better understanding of the complex couplings within the codes are needed before the models could be used with confidence as a predictive tool to assess gas movement.
- **Heterogeneity**: the role of material heterogeneity needs to be further explored, as it has shown that it might provide a possible way to represent flow localisation. Indeed, some teams have assumed heterogeneous fields (e.g., permeability, gas entry pressure), as the introduction of heterogeneity at the capillary scale is not practicable. However, the assumed distribution functions are usually arbitrary prescribed and lack a physical justification. In the absence of data (e.

g., characterisation of pore morphology, variation in material properties), this issue remains a challenge for all teams.
- **Stochasticity**: experimental data exhibits a combination of stochastic and deterministic behaviours. Despite the growing awareness of the need to reflect non-deterministic process features, developed approaches in this study are purely deterministic and hence, it is therefore important for numerical modelling to consider how best to account for key stochastic features such as the number of gas pathways, the precise timing of the gas breakthrough and the associated gas flows.
- **Upscaling**: although this paper presents a summary of the modelling work performed when simulating laboratory-scale experiments, models that are tractable at the engineered barrier and repository scales are needed. Due to the need to accurately and efficiently include small-scale heterogeneities in a field-scale model, this poses a major challenge and will constitute the main aim of the next stage of the D-2023 project. In this forthcoming stage, the modelling of a full-scale in situ test (Lasgit) will be undertaken. This is a highly instrumented test based on a mock canister, encapsulated in bentonite/pellets, and placed within a deposition hole at the Äspö underground research laboratory (Sweden). At the current stage of the modelling study, substantial future work is needed to account for some of the foreseen complexities (e.g., representation of the heterogeneous porous field-scale domain and the inclusion of the interfaces, since they play an important role). However, the expansion of the numerical approaches to a full-scale test will provide an invaluable insight to help to inform the modelling approaches and assess the impact of upscaling of gas flow on repository layout and therefore the design of any future facility.
- **Application**: the validity of these models for the prediction of gas flow in repository systems remains limited. Upscaling the detailed processes represented in the current models would be computationally challenging, requiring compromises in both mesh density and simplification, or, averaging of less important processes. However, it is important to remember that models need only to be fit for their application, so long as end-users clearly understand their deficiencies. Any changes/simplifications to the models would require experimental validation where possible and be derived from a detailed understanding of the importance/relevance of key phenomenological features.

6. Conclusions

Different numerical representations for the quantitative description of advective gas flow in clay-based repository systems have been developed. This study shows that models that are used to simulate particular controlled-laboratory experiments (Task A in the D-2019 project) can be employed to reproduce other tests, even with different sample geometries.

This study has also shown that these numerical approaches can successfully represent some of the main deterministic experimental features typically observed in dilatancy-controlled gas flow (e.g., initial and peak stress values). However, there are other features that are not correctly captured (e.g., rapid transition phase seen at breakthrough). This suggests that numerical models still lack a correct description of the full complexity of the physical processes observed in water-saturated experiments.

This study has identified three key learning points that need to be born in mind when numerically modelling gas flow through water saturated low permeable clay samples:

1. **Model calibration**: models need calibration of fitted parameters. Each model needs a specific calibration process and thus, their adjustment requires detailed sensitivity analysis. Since gas flow is semi-stochastic by nature, these analyses should distinguish between

the key experimental features reproducible across all experiments and those that only occur in specific experiments.

2. **Heterogeneity**: preferential pathways are not explicitly represented and hence, fracture-specific properties such as the evolving fracture front are not included into the models. Instead, heterogeneous material distributions can be used to implicitly represent preferential pathways.

3. **Model coarsity**: developed models are not fine enough to include microscopic dilatancy or heterogeneous gas channelling. Although this might represent a limitation, the use of fine meshes is not recommended, as approaches that can potentially be tractable at engineered barrier and repository scales are ultimately needed.

CRediT authorship contribution statement

E. Tamayo-Mas: supervision, validation, writing – original draft. **J. F. Harrington**: supervision, validation, data acquisition, writing – review and editing, funding acquisition. **I. P. Damians, S. Olivella, E. Radeisen, J. Rutqvist, Y. Wang**: model development, writing – review and editing.

Declaration of Competing Interest

The authors declare that they have no known competing financial

interests or personal relationships that could have appeared to influence the work reported in this paper.

Data Availability

Approaches have been assessed against a new and hitherto unpublished gas test. A brief overview of the experimental data is given in the manuscript. Data might be made available on request.

Appendix A. model comparison

Differences between the proposed numerical strategies lie in conceptual features, the software used by the teams, in the assumed geometry to represent the saturated bentonite, in the initial/boundary conditions prescribed for the tests and in the material parameters. Here, these differences are reported.

Conceptual differences between the numerical strategies

Table 5
Brief description of the three numerical models developed by the participating teams.

	BGR/UFZ	LBNL	CIMNE-UPC/Andra
Hydro-mechanical (HM) coupling	Fully coupled (via the Biot's effective stress tensor) HM model	Sequentially coupled (via the Biot's effective stress tensor) HM model	Fully coupled (via the Biot's effective stress tensor) HM model
Key hydraulic features	Van Genuchten- Mualem model	Van Genuchten- Corey model	Fracture-dependent van Genuchten model + fracture-dependent relative permeabilities
Mechanical deformation	Elasto-plasticity (Drucker-Prager with a tension cut-off parameter)	Linear elasticity (with swelling stress)	Elasticity (with a dilatancy term in the deviatoric component of the volumetric strains)
Dilatant pathways description	Strain-dependent intrinsic permeability triggered by a heterogeneous Young's modulus	Permeability is assumed to depend on pressure and the effective minimum compressive stress	Intrinsic and relative permeabilities are assumed to be decomposed into matrix and fracture terms

Codes used by the teams

Table 6
Software employed by the participating teams.

	BGR/UFZ	LBNL	CIMNE-UPC/Andra
Software	OpenGeoSys	TOUGH2 + FLAC^{3D}	CODE_BRIGHT
Version	5.8	TOUGH2 V2.1 FLAC3D V5	8.6
Reference	[38]	[45] + [46]	[48]

Test geometries used by the teams

Table 7
Test geometries employed by the teams.

	BGR/UFZ	LBNL	CIMNE-UPC/Andra
Discretisation method	Finite element	Integral finite difference	Finite element
Geometry	2D triangular axisymmetric mesh	3D quadrilateral axisymmetric mesh	3D hexahedral mesh
Number of elements	2716	857	3430
Number of nodes	1448	1846	3909
Explicit description of the injector	Via a source term	Via a representative volume of the injection chamber	With all the relevant components (i.e., injection rod and injection filter tip)
Element order	2nd order (quadratic triangular)	Linear	Linear

Prescribed initial conditions

Table 8
Initial conditions prescribed by the teams.

	BGR/UFZ	LBNL	CIMNE-UPC/Andra
Pore-water pressure (MPa)	1.00	1.00	0.25
Pore-gas pressure (MPa)	3.00	1.00	0.10
Water saturation	97%	100%	100%
Swelling pressure	Compressive stress: no real swelling	8.0	-
Capillary pressure (MPa)	2.0	0.0	0.0
Displacements along x axis	-	0.0	0.0
Displacement along y axis	-	0.0	0.0
Displacements along z axis (if appropriate)	-	0.0	0.0
Stress (MPa)	7.0 (effective compressive stress)	8.0	8.0
Temperature	20°	20°	20°

Prescribed boundary conditions

Table 9
Boundary conditions prescribed by the teams.

	BGR/UFZ	LBNL	CIMNE-UPC/Andra
Pore-water pressure	-	1 (at outlet)	Variable (as per given test specifications)
Pore-gas pressure (MPa)	1 (top of sample, outflow)	1 (at outlet)	Variable (as per given test specifications)
Flowrate injector	$\dot{m}(t) = \frac{nV_0}{\Delta V_{In,t}}$	Prescribed until 85 days to match injection pressure rise	Prescribed from 22 to 85 days as per test Flow rate at STP plot given
Capillary pressure	-	0 at outlet/inlet	Variable (as per given test specifications)
Displacements along x axis	Right boundary = 0 Left boundary = symmetry axis	0 normal to outer surface	0 at all outer surfaces
Displacement along y axis	Top and bottom boundary = 0	0 normal to outer surface	0 at all outer surfaces
Displacements along z axis (if appropriate)	-	0 normal to outer surface	0 at all outer surfaces
Temperature	20°	20°	20°

Final parameter values employed by the teams

The basic material parameters employed by the teams are listed and compared in Table 10. Specific model parameters that need to be calibrated (or that are considered known) are reported in following sections.

Table 10
Basic parameters used by the teams (* indicates values beyond specified parameters).

	BGR/UFZ	LBNL	CIMNE-UPC/Andra
Elastic modulus (MPa)	Heterogeneous*	307	307
Poisson's ratio (-)	0.4	0.4	0.4

Table 10 (*continued*)

	BGR/UFZ	LBNL	CIMNE-UPC/Andra
Porosity (-)	0.43 *	0.44	0.4327 (initial porosity)
Biot's coefficient (-)	0.9	1	0.5
Intrinsic permeability of water (m^2)	3.0×10^{-20} *	3.4×10^{-21}	Heterogeneous*

Parameters employed by BGR/UFZ

Table 11
Calibrated parameters employed by BGR/UFZ.

Parameter	Symbol	Units	Calibrated value	Sensitivity analysis		Effect with respect to the global response
				Minimum value	Maximum value	
Plastic strain multiplier	b_1	-	4000	1000	4000	Impacts the intrinsic permeability
Volumetric strain multiplier	b_3	-	250	50	250	Impacts the intrinsic permeability
Intrinsic permeability	k_{in}	m^2	7.0×10^{-21}	3.0×10^{-21}	6.0×10^{-20}	Impacts the breakthrough time and the total flow
Mean of the Young's modulus distribution	$\bar{E}$	Pa	3.5×10^9	4.5×10^8	3.5×10^9	Impacts the breakthrough time
Minimum value of the Young's modulus distribution	E_{min}	Pa	5.0×10^8	-	-	Impacts the breakthrough time

Table 12
Other parameters (assumed known) employed by BGR/UFZ to characterise the bentonite.

Parameter	Symbol	Units	Calibrated value	Taken from
Density of solid grains	ρ_s	kg/m^3	1570	Decovalex 2019[21]
Friction angle	φ	°	32	-
Dilatancy angle	ψ	°	20	-
Cohesion	c	MPa	3	-
Tortuosity	τ	-	1	-
Apparent gas entry pressure (van Genuchten model)	P_0	MPa	10	[A.1]
Measure of the pore size distribution (van Genuchten model)	n	-	1.49	[A.2]
Residual degree of saturation (van Genuchten model)	S_{res}	-	0.01	[A.1]
Maximum degree of saturation (van Genuchten model)	S_{max}	-	0.99	[A.1]

Parameters employed by LBNL

Table 13
Calibrated parameters employed by LBNL.

Parameter	Symbol	Units	Calibrated value	Sensitivity analysis		Effect with respect to the global response
				Minimum value	Maximum value	
Swelling coefficient	β_{sw}	-	0.015	0.01	0.03	Impacts the total stress level
Max aperture for stress-permeability	b_{h0}	m	4.9×10^{-6}	1.0×10^{-7}	1.0×10^{-5}	Impacts gas flow rate after break through
Reference stress normal to the fracture	$\sigma_{n.ref}$	Pa	0.1	0.05	1.0	Impacts gas flow rate after break through
Residual saturation of gas (Corey model)	S_{gr}	-	0.13	0.05	0.2	Impacts gas entry (pressure)
Multiplying factor for the enhanced gas permeability (Corey model)	m_g	-	375	100	1000	Impacts gas flow rate

Table 14
Other parameters (assumed fixed) employed by LBNL.

Parameter	Symbol	Units	Calibrated value	Taken from
Apparent gas entry pressure (van Genuchten model)	P_0	MPa	18	[41]
Shape factor (van Genuchten model)	λ	-	0.45	[41]
Residual liquid saturation (van Genuchten model)	S_{lr}	-	0.01	[41]

Parameters employed by CIMNE-UPC/Andra

Table 15
Other parameters (assumed fixed) employed by CIMNE-UPC/Andra.

Parameter	Symbol	Units	Calibrated value	Taken from
Homogeneous part (same parameter value for the entire sample modelled)				[21]
Dilatancy angle	ψ	°	24	
Tortuosity for dissolved gas (Fick's law)	τ	-	0.5	
Transverse dispersion coefficient (Fick's law)	D_T	-	0.001	
Longitudinal dispersion coefficient (Fick's law)	D_L	-	0.01	
Power for liquid state for both matrix and fractures (Relative permeability)	$n_{liquid}^{matrix/fractures}$	-	3	
Maximum liquid saturation (Relative permeability)	S_{liquid}^{max}	-	1	
Minimum liquid saturation (Relative permeability)	S_{liquid}^{min}	-	0	
Power for gas state for matrix (Relative permeability)	n_{gas}^{matrix}	-	2	
Power for gas state for fractures (Relative permeability)	$n_{gas}^{fractures}$	-	1	
Maximum gas saturation (Relative permeability)	S_{gas}^{max}	-	0.3	
Minimum gas saturation (Relative permeability)	S_{gas}^{min}	-	0	
Shape function (van Genuchten model	λ_{VG}	-	0.45	
Initial porosity	ϕ_0	-	0.44	
Dry density	ρ_{dry}	kg/m^3	1512	
Molar mass of Helium	M	kg/mol	0.004	
Henry's constant	H	MPa	10000	
Heterogeneous part (three different sample zones randomly distributed). M1 (2/3) - M2 (1/6) - M3 (1/6), seeFig. 16.				[21]
Initial capillary pressure (van Genuchten model)	P_0	MPa	M1: 48.6	
			M2: 22.5	
			M3: 10.8	
Finite air entry value	P_{00}	MPa	M1: 5.4	
			M2: 2.5	
			M3: 1.2	
Reference permeability (matrix intrinsic permeability)	k_0	m^2	M1: 1.0×10^{-21}	
			M2: 1.0×10^{-20}	
			M3: 1.0×10^{-19}	
Internal associated width for each fracture	a	m	M1: 5.0×10^{-6}	
			M2: 5.0×10^{-5}	
			M3: 5.0×10^{-4}	
Initial aperture of the fractures	b_0	m	M1: 1.5×10^{-9}	
			M2: 5.0×10^{-9}	
			M3: 9.5×10^{-9}	
Maximum aperture of the fractures	b_{max}	m	M1: 1.5×10^{-7}	
			M2: 3.5×10^{-7}	
			M3: 7.5×10^{-7}	
Initial strain	ε_0	%	M1: 0.05	
			M2: 0.03	
			M3: 0.01	

A. 7 Appendix references.

[A.1] R. Senger, E. Romero, A. Ferrari and P. Marschall (2014). Characterization of gas flow through low-permeability claystone: laboratory experiments and two-phase flow analyses. *Geological Society, London, Special Publications,* 400, 1, pp. 531–543. DOI: 10.1144/SP400.15.

[A.2] Z. Dai, J. Samper, A. Wolfsberg and D. Levitt (2008). Identification of relative conductivity models for water flow and solute transport in unsaturated bentonite. *Physics and Chemistry of the Earth, Parts A/B/C,* 33, 1, pp. S177-S185. DOI: 10.1016/j.pce.2008.10.012.

Appendix B. new theoretical model developed by SNL

SNL developed an alternative approach to describe the key features observed in gas-laboratory tests that distinguish clay-rich media from other rock-types.

The new model expands the work performed in [B.1], where a phenomenological concept of nonlinear dynamics and deterministic chaos theory was employed to analyse the gas pressure and the gas influx and outflux obtained from a one-dimensional test performed on a pre-compacted Mx80 bentonite sample at the British Geological Survey. Indeed, the computation of a set of diagnostic parameters [e.g., global embedding dimension, correlation dimension, information dimension, spectrum of Lyapunov exponents (B.1. and references therein)] suggested that the prevailing processes during the gas test are (i) chaotic diffusion both at the onset of gas influx and during the final phase of the experiment and (ii) chaotic advection after the breakthrough. The time series analyses of the data indicate that the observed chaotic behaviour of the system can be described by 3–5 independent variables. Here, focus is placed on the development of a conceptual model for such chaotic systems. A detailed mathematical formulation and analysis will be provided elsewhere.

The primary research focus of the SNL team within the current D-2023 project is to understand the actual mechanism(s) for the emergence of the observed complex behaviour of gas migration in water saturated compact bentonite. In particular:

- **Channelling postulate**: although gas migration in a porous medium is generally treated as an immiscible displacement process within a "rigid" solid framework, this is unlikely to be the case for hydrated compacted bentonite, where the pore size is generally extremely small (on a scale of nanometers). Indeed, the capillary pressure p_c in such a medium can be estimated by

$$p_c = \frac{2\sigma\cos(\theta)}{r} \tag{19}$$

where σ (N/m) is the surface tension between gas and water, θ (°) is the contact angle water on the solid; and r (m) is the radius of the pore necks. Typical values of these parameters ($\sigma = \sim70$ mN/m, $\theta = \sim40°$, $r = 1$ - 10 nm, see [B.2] and [B.3]) lead to a significantly higher p_c (~10 - 100 MPa) than the gas pressure generally used in experiments and therefore, given the low tensile strength of bentonite, the only possible way for gas to move through such a medium is by channelling.

- **Channelling description**: this channelling process is mathematically analogous to the buoyant rising of a viscous fluid within another viscous fluid, [B.4]. This allows the characterisation of both the spacing of channels

$$\lambda = \frac{2\pi L_1}{3^{1/3}}\left(\frac{\mu_2}{\mu_1}\right)^{1/3} \tag{20}$$

and the perturbation growth of the interface

$$\xi = \frac{2\Delta P_g L_1}{3(L_1 + L_2)\mu_2}\left(\frac{\mu_2}{24\mu_1}\right)^{1/3} \tag{21}$$

where μ_1 and μ_2 are the viscosities of gas and water-saturated compacted bentonite (Pa·s) respectively, ΔP_g (Pa) is an externally imposed gas pressure gradient and L_1, L_2 (m) are the lengths defined in Fig. 23[A], characterising the compressibility of the bentonite, which is in turn related to the swelling pressure of bentonite as a function of the dry density of the material.

As seen in Eq. (20), the spacing of channels only depends on the viscosity ratio μ_2/μ_1 and the length L_1. Hence, the number of channels to be developed in the system is determined by the viscosity ratio only, see Fig. 23[C]. Moreover, it is interesting to note that the spacing of channels is linearly proportional to the length L_1, implying that the channeling mechanism is linearly scalable. In other words, the complex fluid flow behaviour in gas migration in bentonite observed in small-scale experiments can probably occur in a large-scale experiment in the field, as highlighted by the multiple gas tests experiments performed within the Lasgit project.

- **Gas breakthrough postulate**: SNL postulates that the breakthrough point of gas migration corresponds to the time when a fully percolating channel network is established across the material domain. One important constraint on the establishment of such networks is that the gas pressure must be high enough to make enough room for gas percolation by compressing the bentonite matrix. The room available for gas migration is directly determined by the swelling capacity of the material and the dry density used in the testing, and thus the breakthrough pressure is around the swelling pressure. Since this room is usually a small fraction of the total material volume in a test, the apparent gas saturation degree is expected to be small.

- **Gas movement postulate (after the channel network is created)**: as experimentally and theoretically shown in [B.4], if the upwelling material has greater viscosity than the surrounding material, the structure is a long vertical column with gradually decreasing diameter and, if the upwelling material has less viscosity than the surrounding material, the structure envelops a rim syncline and a pronounced overhang and eventually ascends as a spherical pocket of fluid fed by a pipe, see Fig. 24. Analogously, and due to the large contrast in viscosity between the bentonite matrix and the gas injected, SNL postulates that gas percolates through a water saturated bentonite matrix in the form of individual gas bubbles. The size of bubbles is determined by the apparent surface tension of the gas-bentonite interface.

- **Gas movement description (after the channel network is created)**: previous work carried out by SNL in [B.5] uses a logistic map model to describe the movement of a gas bubble in a deformable clay matrix which can display a complex dynamic behaviour that can be explained with a bifurcation and chaos concept. Indeed, the dynamic behaviour of the system has been shown closely related to clay matrix dilation, fracturing and fracture healing as induced by gas bubble movement. Therefore, these components should be included in any model describing the advective movement of gas through low-permeability materials.
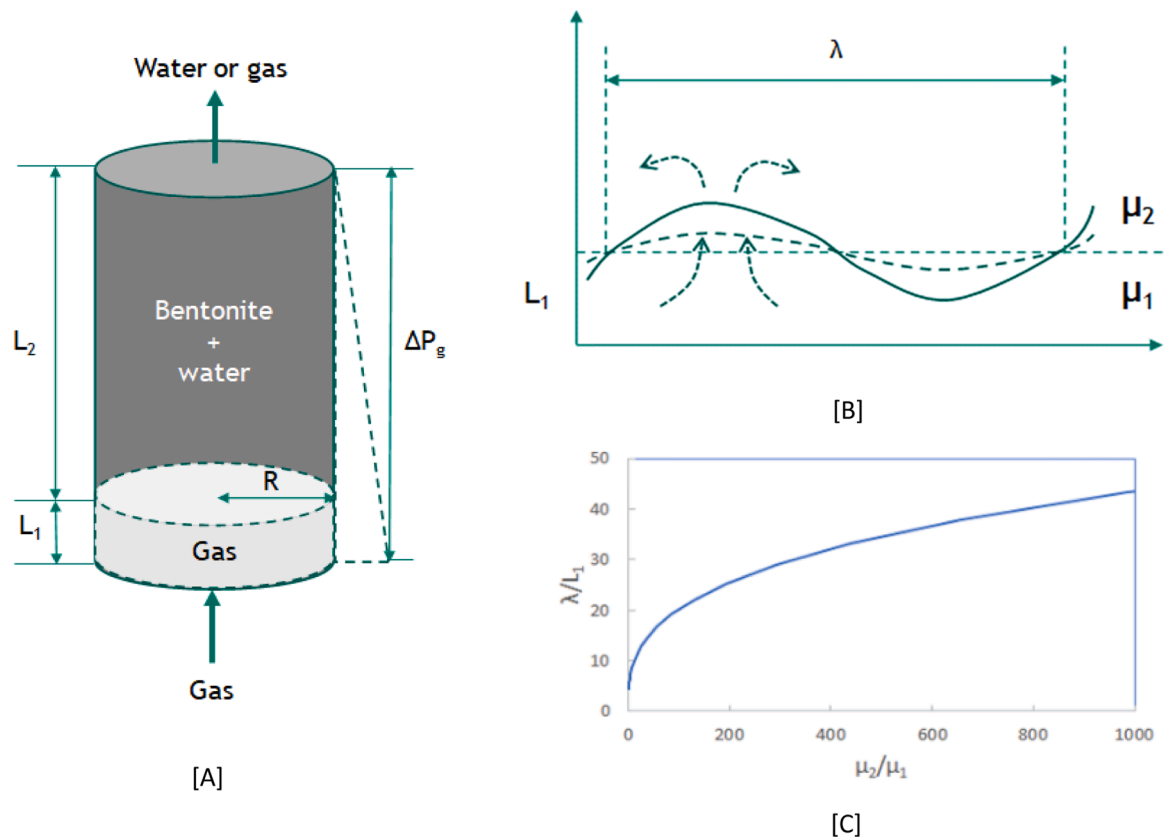
Fig. 23. Stability analysis of gas-water saturated bentonite interface: [A] modelling system, [B] perturbation growth of the interface and [C] spacing of channels determined by the viscosity ratio.
.

B.1. Appendix references

[B.1] B. Faybishenko, Y. Wang, J.F. Harrington, E. Tamayo-Mas, J. Birkholzer and C. Jové -Colón (2022). Phenomenological Model of Nonlinear Dynamics and Deterministic Chaotic Gas Migration in Bentonite: Experimental Evidence and Diagnostic Parameters. *Transport in Porous Media,* 141, p. 585–606. DOI: 10.1007/s11242–021-01733–9.

[B.2] Y. Wang, C. Bryan, T. Dewers, J.E. Heath and C. Jove-Colon (2012). Ganglion Dynamics and Its Implications to Geologic Carbon Dioxide Storage. *Environmental Science and Technology,* 47, 1, p. 219–226. DOI: 10.1021/es301208k.

[B.3] Y. Wang (2014). Nanogeochemistry: Nanostructures, emergent properties and their control on geochemical reactions and mass transfers. *Chemical Geology,* 378–379, pp. 1–23. DOI: 10.1016/j.chemgeo.2014.04.007.

[B.4] J.A. Whitehead Jr and D.S. Luther (1975). Dynamics of laboratory diapir and plume models. *Journal of Geophysical Research,* 80, 5, pp. 705–717. DOI: 10.1029/JB080i005p00705.

[B.5] Y. Wang, T. Hadgu, E. Kalinina, C. Jove-Colon and B. Faybishenko (2018). International Collaboration on Spent Fuel Disposition in Crystalline Media: FY18 Progress Report. DOI: 10.2172/1469442.

References

1. Sellin P, Leupin OX. The use of clay as an engineered barrier in radioactive-waste management–a review. *Clays Clay Miner.* 2013;61(6):477–498. https://doi.org/10.1346/CCMN.2013.0610601.

2. Shirazi SM, Kazama H, Salman FA, Othman F, Akib S. Permeability and swelling characteristics of bentonite. *Int J Phys Sci.* 2010;5(11):1647–1659.

3. Daniels KA, Harrington JF, Zihms SG, Wiseall AC. Bentonite permeability at elevated temperature. *Geosciences.* 2017;7(1):3. https://doi.org/10.3390/geosciences7010003.

4. Harrington JF, Volckaert G, Noy DJ. Long-term impact of temperature on the hydraulic permeability of bentonite. *Lond: Geol Soc Lond.* 2014;400:589–601. https://doi.org/10.1144/SP400.31.

5. Dixon DA, Stone J, Birch K, Kim CS. Sealing materials for a deep geological repository: Evaluation of swelling pressure and hydraulic conductivity data for bentonite-based sealing materials proposed for use in placement rooms. *Can Geotech J.* 2023;60(7):951–965. https://doi.org/10.1139/cgj-2021-0609.

6. Li KP, Chen YG, Ye WM, Wang Q. Self-sealing behavior of bentonite-based materials in high-level radioactive waste disposal: A systematic review, 106873 *Appl Clay Sci.* 2023;235(106873):2023. https://doi.org/10.1016/j.clay.2023.106873.

7. Harrington JF, Daniels KA, Wiseall AC, Sellin P. Bentonite homogenisation during the closure of void spaces. *Int J Rock Mech Min Sci.* 2020;136, 104535. https://doi.org/10.1016/j.ijrmms.2020.104569.

8. International Atomic Energy Agency (1997). Experience in Selection and Characterization of Sites for Geological Disposal of Radioactive Waste, *IAEA TECDOC-991*, IAEA, Vienna.

9. W.R. Rodwell, A.W. Harris, S.T. Horseman, P. Lalieux, W. Müller, L. Ortiz Amaya, K. Pruess (1999). Gas Migration and Two-phase Flow through Engineered and Geological Barriers for a Deep Repository for Radioactive Waste: a Joint EC/NEA Status Report (Nuclear Science and Technology). *EC Report EUR19122.* European Commission, Luxembourg.

10. Horseman ST, Harrington JF, Sellin P. Gas migration in MX80 buffer bentonite. *MRS Online Proc Libr.* 1996;465:1003–1010. https://doi.org/10.1557/PROC-465-1003.

11. J.F. Harrington, S.T. Horseman (2003). Gas migration in KBS-3 buffer bentonite. Sensitivity of test parameters to experimental boundary conditions. Technical Report TR-03–02. Svensk Kärbränslehantering AB (SKB), Stockholm, Sweden.

12. Harrington JF, Milodowski AE, Graham CC, Rushton JC, Cuss RJ. Evidence for gas-induced pathways in clay using a nanoparticle injection technique. *Mineral Mag.* 2012;76(8):3327–3336. https://doi.org/10.1180/minmag.2012.076.8.45.

13. Cuss RJ, Harrington JF, Giot R, Auvray C. Experimental observations of mechanical dilation at the onset of gas flow in Callovo-Oxfordian claystone. *Lond: Geol Soc Lond.* 2014;400:507–519. https://doi.org/10.1144/SP400.26.

14. Cuss RJ, Harrington JF, Noy DJ, Graham CC, Sellin P. Evidence of localised gas propagation pathways in a field-scale bentonite engineered barrier system; results from three gas injection tests in the Large scale gas injection test (Lasgit). *Appl Clay Sci.* 2014;102:81–92. https://doi.org/10.1016/j.clay.2014.10.014.

15. Harrington JF, Graham CC, Cuss RJ, Norris S. Gas network development in a precompacted bentonite experiment: Evidence of generation and evolution. *Appl Clay Sci.* 2017;147:80–89. https://doi.org/10.1016/j.clay.2017.07.005.

16. Graham CC, Harrington JF, Sellin P. Gas migration in pre-compacted bentonite under elevated pore-water pressure conditions. *Appl Clay Sci.* 2016;132:353–365. https://doi.org/10.1016/j.clay.2016.06.029.

17. Harrington JF, Graham CC, Cuss RJ, Norris S. Gas network development in compact bentonite: key controls on the stability of flow pathways. *Geofluids.* 2019;2019:1–19. https://doi.org/10.1155/2019/3815095.

18. Xu L, Ye WM, Ye B, Chen B, Chen YG, Cui YJ. Investigation on gas migration in saturated materials with low permeability. *Eng Geol.* 2015;197:94–102. https://doi.org/10.1016/j.enggeo.2015.08.019.

19. Cui LY, Ye WM, Wang Q, Chen YG, Chen B. Gas migration behavior in saturated bentonite under flexible conditions with consideration of temperature effects. *Acta Geotech.* 2023;18(2):971–984. https://doi.org/10.1007/s11440-022-01624-3.

20. Senger R, Romero E, Marschall P. Modeling of gas migration through low-permeability clay rock using information on pressure and deformation from fast air injection tests. *Transp Porous Media.* 2018;123:563–579. https://doi.org/10.1007/s11242-017-0962-5.

21. Tamayo-Mas E, Harrington JF, Brüning T, et al. Modelling advective gas flow in compact bentonite: lessons learnt from different numerical approaches. *Int J Rock Mech Min Sci.* 2021;139, 104580. https://doi.org/10.1016/j.ijrmms.2020.104580.

22. Guo G, Fall M. Modelling of dilatancy-controlled gas flow in saturated bentonite with double porosity and double effective stress concepts. *Eng Geol.* 2018;243: 253–271. https://doi.org/10.1016/j.enggeo.2018.07.002.

23. Radeisen E, Shao H, Hesser J, Kolditz O, Xu W, Wang W. Simulation of dilatancy-controlled gas migration processes in saturated bentonite using a coupled multiphase flow and elastoplastic H2M model. *J Rock Mech Geotech Eng.* 2023;15(4): 803–813. https://doi.org/10.1016/j.jrmge.2022.05.011.

24. Chittenden N, Benbow S, Bond A, Norris S. Development of an upscalable HM model for representing advective gas migration through saturated bentonite. *Int J Rock Mech Min Sci.* 2020;133, 104415. https://doi.org/10.1016/j.ijrmms.2020.104415.

25. Yang J, Fall M. Coupled hydro-mechanical modelling of dilatancy controlled gas flow and gas induced fracturing in saturated claystone. *Int J Rock Mech Min Sci.* 2021;138, 104584. https://doi.org/10.1016/j.ijrmms.2020.104584.

26. Damians IP, Olivella S, Gens A. Modelling gas flow in clay materials incorporating material heterogeneity and embedded fractures. *Int J Rock Mech Min Sci.* 2020;136, 104524. https://doi.org/10.1016/j.ijrmms.2020.104524.

27. K.A. Daniels, J.F. Harrington (2017). The response of compact bentonite during a 1D gas flow test. British Geological Survey Open Report. OR/17/067.

28. T. Manai (1995). EVEGAS: European validation exercise of GAS migration models through geological media: Phase 1 - Final Report. European Commission Report EUR 16639 EN. European Commission, Nuclear Science and Technology Series, Directorate-General, Science, Research and Development, Luxembourg.

29. T. Manai (1997). EVEGAS: European validation exercise of gas migration models through geological media: Phase 2 - Final Report. European Commission Report EUR 17556 EN. European Commission, Nuclear Science and Technology Series, Directorate- General, Science, Research and Development, Luxembourg.

30. T. Manai (1997). EVEGAS: European validation exercise of gas migration models through geological media: Phase 3 - Final Report. European Commission Report EUR 17557 EN. European Commission, Nuclear Science and Technology Series Directorate- General, Science, Research and Development, Luxembourg.

31. P.J. Nash, B.T. Swift, M. Goodfield, W.R. Rodwell (1998). Modelling Gas Migration in Compacted Bentonite: A report produced for the GAMBIT Club. POSIVA Report 98–08. Posiva Oy, Helsinki.

32. B.T. Swift, A.R. Hoch, W.R. Rodwell (2001). Modelling Gas Migration in Compacted Bentonite: GAMBIT Club Phase 2 Final Report. POSIVA Report 2001–02. Posiva Oy, Olkiluoto.

33. A.R. Hoch, K.A. Cliffe, B.T. Swift, W.R. Rodwell (2004). Modelling Gas Migration in Compacted Bentonite: GAMBIT Club Phase 3 Final Report. POSIVA Report 2004–2. Posiva Oy, Olkiluoto.

34. van Genuchten MT. A closed-form equation for predicting the hydraulic conductivity of unsaturated soils. *Soil Sci Soc Am J.* 1980;44(5):892–898. https://doi.org/10.2136/sssaj1980.03615995004400050002x.

35. Biot MA, Willis DG. The elastic coefficients of the theory of consolidation. *J Appl Mech.* 1957;24(4):594–601. https://doi.org/10.1115/1.4011606.

36. Villar MV, Iglesias RJ, García-Siñeriz JL. State of the in situ Febex test (GTS, Switzerland) after 18 years: a heterogeneous bentonite barrier. *Environ Geotech.* 2018;7(2):147–159. https://doi.org/10.1680/jenge.17.00093.

37. W.J. Xu, H. Shao, H. Hesser, W.Q. Wang, O. Kolditz, T. Popp (2011). Simulation of dilatancy-controlled gas migration process in saturated argillaceous rock. *Proceedings of the 2nd International Symposium on Computational Geomechanics (Comgeo II),* Cavtat-Dubrovnik.

38. Kolditz O, Bauer S, Bilke L, et al. OpenGeoSys: an open-source initiative for numerical simulation of thermo-hydro-mechanical/chemical (THM/C) processes in porous media. *Environ Earth Sci.* 2012;67(2):589–599. https://doi.org/10.1007/s12665-012-1546-x.

39. Gray WG, Hassanizadeh SM. Unsaturated flow theory including interfacial phenomena. *Water Resour Res.* 1991;27(8):1855–1863. https://doi.org/10.1029/91WR01260.

40. Kunhwi K, Rutqvist J, Harrington JF, Tamayo-Mas E, Birkholzer JT. Discrete dilatant pathway modeling of gas migration through compacted bentonite clay. *Int J Rock Mech Min Sci.* 2021;137, 104569. https://doi.org/10.1016/j.ijrmms.2020.104569.

41. R.K. Senger, P. Marschall (2008). Task Force on EBS/Gas Transport in Buffer Material. NAGRA NAB 08–24, Wettingen, Switzerland.

42. Rutqvist J, Ijiri Y, Yamamoto H. Implementation of the Barcelona Basic Model into TOUGH-FLAC for simulations of the geomechanical behavior of unsaturated soils. *Comput Geosci.* 2011;37:751–762. https://doi.org/10.1016/j.cageo.2010.10.011.

43. Bandis SC, Lumsden AC, Barton NR. Fundamentals of rock joint deformation. *Int J Rock Mech Min Sci Geomech Abstr.* 1983;20(6):249–268. https://doi.org/10.1016/0148-9062(83)90595-8.

44. Rutqvist J. An overview of TOUGH-based geomechanics models. *Comput Geosci.* 2017;108:56–63. https://doi.org/10.1016/j.cageo.2016.09.007.

45. Pruess K, Oldenburg C, Moridis G. TOUGH2 user's guide, version 2.1, LBNL-43134 (revised). *Berkeley, USA: Lawrence Berkeley Natl Lab.* 2012.

46. Itasca (2018). FLAC3D VERSION 6.0. Fast Lagrangian Analysis of Continua in 3 Dimensions. ITASCA Consulting Group Inc.

47. Olivella S, Alonso EE. Gas flow through clay barriers. *Géotechnique.* 2008;58(3): 157–176. https://doi.org/10.1680/geot.2008.58.3.157.

48. Olivella S, Gens A, Carrera J, Alonso EE. Numerical formulation for simulator (CODE_BRIGHT) for coupled analysis of saline media. *Eng Comput.* 1996;13(7): 87–112. https://doi.org/10.1108/02644409610151575.

49. I.P. Damians, B.S. Noghretab, S. Olivella, A. Gens (2022). Numerical Mesh Sensitivity Works Performed to Analyze Advective Gas Flow in a Compact Clay. Paper presented at the 56th U.S. Rock Mechanics/Geomechanics Symposium, Santa Fe, New Mexico, USA, June 2022. ⟨doi:10.56952/ARMA-2022–0679⟩.